TECHNISCHE
UNIVERSITÄT
WIEN

DIPLOMARBEIT

Economic eye length measurements for point of care diagnostics, implementing a custom-made balanced detector

zur Erlangung des akademischen Grades

Diplom-Ingenieurin

im Rahmen des Studiums

Biomedical Engineering

eingereicht von

Milana Kendrisic
Matrikelnummer 01227315

ausgeführt am Institut für Angewandte Physik
der Fakultät für Physik der Technischen Universität Wien
in Zusammenarbeit mit der Medizinischen Universität Wien

Betreuung
Ao.Univ.Prof. Dr. Rainer Leitgeb
Ao.Univ.Prof. Dr. Martin Gröschl

Wien, 16.12.2019

(Unterschrift Verfasserin)

(Unterschrift Betreuer)

Abstract

Cataract surgery is one of the most frequent surgical procedures performed worldwide. Optical biometry measurements are crucial for performing successful surgical removal of the eye lens, and its replacement with an artificial one. In developing countries, economic inaccessibility of biometric devices is one of the main obstacles for curing blindness caused by cataracts. Research has shown that electrically tuned vertical-cavity edge-emitting laser diodes (VCSEL) have sufficient coherence length and therefore the potential for performing low-cost eye length measurements. This study aims to determine whether more economic solutions can be used for VCSEL laser tuning and laser beam detection.

A laser driver electronic module by Analog technologies was integrated into the optical setup. The maximum tuning range of a VCSEL was examined using a spectrometer. In comparison with a commercial laser driver, a low-cost laser driver consumed less power while achieving the same VCSEL tuning range (spectral bandwidth) of 8.5 nm.

Furthermore, a custom-made balanced detector circuit was designed and tested in-vivo on a healthy volunteer. The resulting axial length measurements have shown a discrepancy of 300 μm between the custom balanced detector and the IOL Master 500. Although the results are promising, further measurements on various subjects need to be performed in order to determine the precision of the custom detector.

In addition, it was brought into question whether a Raspberry Pi 3B+ microcomputer is suitable for performing simultaneous signal transmission and signal acquisition. The results have shown that the lack of acquisition stability as well as the insufficient acquisition speed make Raspberry Pi a non-fitting choice for the task.

Kurzfassung

Die Kataraktoperation ist heute eine der häufigsten Operationen weltweit. Dabei sind optische Biometriemessungen entscheidend für die erfolgreiche chirurgische Entfernung der Augenlinse und deren Ersatz durch eine künstliche Linse. In Entwicklungsländern ist die wirtschaftliche Unzugänglichkeit von biometrischen Geräten eines der Haupthindernisse für die Vermeidung der durch Katarakte verursachten Erblindung. Untersuchungen haben gezeigt, dass Oberflächenemitter (Vertical-Cavity Surface-Emitting Laser, VCSEL) eine ausreichende Kohärenzlänge aufweisen und daher grundsätzlich die Möglichkeit bieten, kostengünstige Augenlängenmessungen durchzuführen. Ziel dieser Studie war es herauszufinden, ob kostengünstigere als die derzeitigen kommerziellen Lösungen für das VCSEL Laser-Tuning und die Laserstrahldetektion verwendet werden können.

Ein Lasertreiber von Analog Technologies wurde in den optischen Aufbau integriert. Der maximale Durchstimmbereich des VCSELs wurde mit einem Spektrometer untersucht. Im Vergleich zu einem kommerziellen Lasertreiber verbraucht ein kostengünstiger Lasertreiber weniger Strom bei gleichem VCSEL Durchstimmbereich (spektrale Bandbreite) von 8.5 nm.

Weiterhin wurde eine speziell angefertigte symmetrische Detektorschaltung entwickelt und in vivo an einem gesunden Freiwilligen getestet. Die durchgeführten axialen Augenlängenmessungen ergaben eine Abweichung von 300 μm zwischen dem in dieser Arbeit entwickelten symmetrischen Detektor und einem kommerziellen IOL Master 500. Obwohl die Ergebnisse vielversprechend sind, müssen weitere Messungen durchgeführt werden, um die Spezifikationen des neuen Detektors zu bestimmen.

Darüber hinaus wurde untersucht, ob ein Raspberry Pi 3B + Mikrocomputer zur gleichzeitigen Signalerfassung und Signalübertragung geeignet ist. Die Ergebnisse haben gezeigt, dass die mangelnde Stabilität sowie die unzureichende Geschwindigkeit den Raspberry Pi für diese Aufgabe ungeeignet erscheinen lassen.

Acknowledgements

The completion of this thesis would not have been possible without the support and guidance that I received from many people.

I would like to express my deep gratitude to Professor Martin Gröschl for his guidance and encouragement. Without his expert advice on electronics, this thesis would not have been achievable.

My deep appreciation also goes out to Professor Rainer Leitgeb for his support, especially in the field of OCT. I am also very grateful to everyone else at the Center for Medical Physics and Biomedical Engineering, especially Laurin Ginner, Lorenzo Ferrara and Michael Niederleithner for their assistance throughout this project.

I gratefully acknowledge the scholarship received from "The Christian Doppler Research Association" for the completion of this thesis.

Finally, I wish to thank my family and Anel for their support and encouragement throughout my studies.

Contents

Chapter 1

Introduction

Vision represents the most precious human sense, 75% of the human perception is based on visual experience, which is by far more than all other senses.[1] Recognition of the visual information in the human brain is a complex process which includes transmission of the light and sensory signal through different parts of the eye and brain. Essentially, the eye lens bends the light rays and focuses them onto the retina, where an electrical signal is generated. As we age, the intraocular lens can become cloudy [1][2], affecting the light refraction and resulting in blurry and obscured vision also called cataract. Therefore, in most cases, the eye lens of the patient is removed and replaced with an artificial lens. Ocular biometry provides highly accurate non-invasive eye length measurements, which are needed for the artificial lens design.[2] Increase in life expectancy results in a progressive increase in the number of cataract surgeries worldwide [3]. Hence, the importance of accessibility of biometric devices increases accordingly.

---

[1] source: https://www.emedicinehealth.com/anatomy_of_the_eye/article_em.htm#eye_anatomy_facts

[2] https://cataract-community.zeiss.com/optical-biometry-explained

Chapter 2

Motivation & State of the Art

As reported by the World Health Organization (WHO) in 2010, cataract is the leading cause of the world blindness (51%), which affects approximately 20 million people.[1] This number is expected to grow, on the account of an increase in life expectancy.
Despite very effective treatment by surgical removal of the clouded lens and replacement with the artificial one, many people in developing countries still become blind from cataract. This happens due to limited access to adequate eye care in their healthcare systems.

The need for economically accessible ocular biometry devices, as well as limitations of ultrasonic biometric devices, due to the risk of infection, motivated this research project. The goal is to develop an economical optical biometry system which is compact, light and portable. Ideally, it is as cheap as possible, and would additionally have to be contactless to ensure maximal hygienic conditions for the patient, and avoid the risk of infection.

The need for high precision and low noise in ocular biometry measurements usually goes hand in hand with utilizing expensive electronics in these kind of systems.

Apart from being costly, most of these devices are also bulky, which prevents them to be easily implementable into a portable compact optical device. Both issues will be addressed in this thesis. It will be investigated whether more affordable electronic modules and custom-made electronics provide results with sufficient precision to potentially be used in ocular biometry devices with the goal of making ophthalmic medical devices available to everyone.

During the course of this research, the goal is to find/build and test alternative solutions for driving a low-cost VCSEL diode and a dual balanced detector.

---

[1] source: World Health Organization https://www.who.int/blindness/causes/priority/en/index1.html

Furthermore, it will be investigated whether these separate parts can be run simultaneously using a microcomputer.

State of the art technology for performing optical biometry is a device called "IOL Master 500"[2], characterized by high precision and good repeatability, confirmed by numerous studies ([4],[5],[6]). However, this device shows to have performance difficulties in patients with mature cataracts. An improved version (IOL Master 700), which uses a swept-source laser is about to appear on the market. A study by Hirnschall ([7] performed in 2018 compared the two versions and concluded that swept-source OCT technology notably improves axial eye length measurements, especially in patients with advanced cataracts, which could not be successfully scanned with the preceding technology. The rate of unsuccessful measurements with the SS-OCT was estimated to be only 0.5%.

Due to the high costs of swept-source lasers, VCSEL-based swept sources for low-cost optical coherence tomography are becoming more popular. A research conducted by Moon and Choi in 2017 [8] concluded that, due to its performance characteristics (low power, narrow tuning range), a swept source VCSEL is not suitable for OCT imaging. Although the tuning range of 10 nm is hardly enough for optical coherence tomography, it may still acceptable for optical biometry.

Furthermore, advancements in computer vision and pattern recognition open many opportunities for low-cost non-invasive measurements, since they may be able to compensate for difficulties in signal acquisition. For example, a study by Poh and McDuff in 2011 [9] has shown that a combination of computer vision and advanced signal processing can be used to calculate heart rate of a person solely from the information from face reflections in a mirror with accuracy of ±3 beats per minute. These results imply that progress in today's technology may be what is needed to bring low-cost healthcare devices closer to being competitive on the market.

---

[2] https://www.zeiss.com/meditec/int/product-portfolio/optical-biometers/iolmaster-500.html

Chapter 3

Basics

3.1 Anatomy of the eye

Functional anatomy of the eye

The human eye is a complex organ, consisting of three different types of tissues - refracting tissue, light sensitive tissue and supporting tissue.

Refracting tissue

The purpose of refracting tissue is to focus light onto the retina. The most important parts of the refractive tissues include: cornea, the pupil, iris, lens, ciliary muscle and vitreous fluid. The different parts of the eye can be seen in Figure 3.1[1]. Light permeability of these structures and adequate lens flexibility are the key conditions for high quality images.

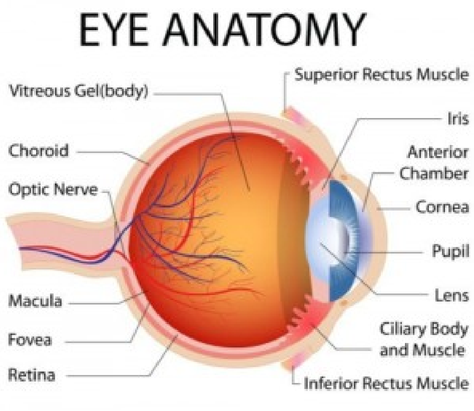

Figure 3.1: Eye Anatomy

---

[1] source: http://arizonaeyes.net/wp-content/uploads/2016/07/eye-anatomy-300x260.jpg

Cornea

Cornea is a transparent tissue structure, situated in the front of the eyeball, which covers the pupil anterior chamber and the iris. Its thickness can vary from the central part (0.5-0.6 mm) to the peripheral part, where it is around 0.7 mm. Its vertical size is 11 mm in adults, while horizontal size is mostly 12 mm[10]. The cornea also has distinct layers, starting from the eye surface (Figure 3.2)[2]:

1. Outer epithelium
2. Basement membrane
3. Bowman layer
4. Stroma
5. Descemet membrane
6. Endothelium

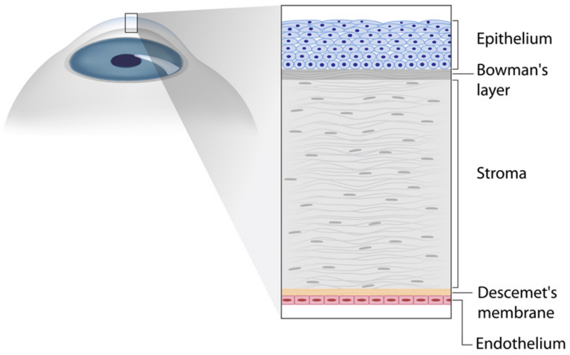

Figure 3.2: Cornea layers

The absence of the blood vessels or lymphatic structures within the corneal tissue enables high light transparency. The main characteristic of outer stratified squamous epithelium is its ability of fast regeneration. Edema or damage of these cells, may cause significant deterioration of the eye sight. The Bowman layer, which can be distinct from the basement membrane is an acellular anterior stroma, consisting of randomly situated collagen fibrils. The stroma is a thick layer, responsible for 90% of total corneal thickness, composed of regularly arranged collagen fibers. The descemet membrane is a basal lamina produced by endothelial cells. The endothelium is an extremely important part of cornea, consisting of cells which cannot be regenerated, that are in charge of dehydration and transparency of stromal tissue[11].

---

[2] source: https://www.eye7.in/wp-content/uploads/illustration-of-structure-of-cornea

Main functions of the cornea

This part of the eye has significant functions regarding protection of the eye against pathogens and harmful substances, as well as focusing power. The cornea is covered with the tear film, which is the major refractive eye surface. Its refractive power is higher than the one of the lens itself, but with a fixed focus[10]. Cornea represents one of the most sensitive tissues in human body, with a high density of pain receptors within it. This characteristic serves as a protection of injury, due to the fact that corneal tissue is mainly non-regenerative.

The pupil, iris, and anterior chamber

The round black whole situated in the center of the iris is called pupil. Size of the pupil is controlled by the iris and dependent of the amount of the light in the room and can vary from 1mm - 10mm in diameter. The color of the pupil is black because light is absorbed by the tissues inside the eye. The iris is a smooth muscle around the pupil. Contraction and relaxation of the iris enables different size of the pupil and different amount of light striking the retina. The space between endothelium of the cornea and iris, filled with aqueous humor is named – the anterior chamber[3]. The cornea, iris, ciliary body and lens are structures which shape the anterior third of the eye, called anterior segment of the eye.

Lens

The biconvex-shaped structure within the eye behind the iris is called lens. It is composed of cells that are transparent and supplied by aqueous humor, as blood vessels inside the lens would deteriorate the vision. The round muscle attached to the lens is called ciliary muscle. Accommodation represents changing the shape of the lens due to contraction and relaxation of ciliary muscle. The process of accommodation enables focusing of the eye on the objects of varying distances[4].

Histology of the crystalline lens

Microanatomy of the lens includes four parts - capsule, epithelium, cortex and nucleus. Acellular capsule represents basement membrane and contains collagen. The lens epithelium is placed posterior to the anterior capsule of the lens in front of the lens fibres. Lens nucleus contains fibres with hexagonal structure in cross-section which enable elasticity of the lens, changing the curvature and accommodation process. Lens cortex is tissue which is surrounding lens cortex

---

[3] source: https://www.emedicinehealth.com/anatomy_of_the_eye/article_em.htm#eye_anatomy_facts

[4] source: https://www.britannica.com/science/lens-eye-structure

without clear separation between cortex and the nucleus. A schematic is shown in Figure 3.3 [5].

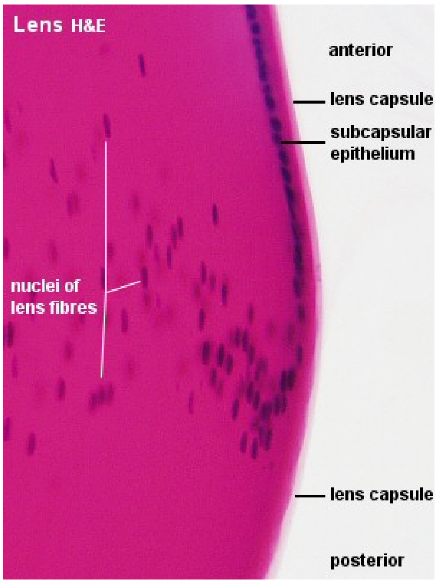

Figure 3.3: Lens histology

Retina

The main part of light sensitive tissue of the eye is the retina. Its structure is depicted in Figure 3.4 [6]. The retina, which covers the internal surface of the eyeball is 0.5 mm thick on average. In the central part of the retina, is the so called optic nerve head, with the origin of numerous blood vessels. It supports the retina with nutrition and is the key part for all nerve cells transporting information to the brain. Close to the optic nerve head, at the distance of 4-5 mm, an avascular, slightly red oval area, called the fovea (macula) is situated.
Inside the retina, 120 million photoreceptor cells are located. Photoreceptor cells can be divided into two main groups: cones and rods. Within these cells, light is transformed into electrical signals. Cones are mainly located in central part of the retina and responsible for color vision in normal light conditions and can be divided into three groups: short (blue), middle (green) and long (red) cones. In the macula there is high density of cones, from all three groups. Therefore, the macula is an important spot in charge for high-acuity vision. The brain is responsible for further processing the signals from different cones to enable distinguishing of different colors. In bright light, mostly cones become activated – this is called photopic vision. Rods are extremely sensitive to light, located

---

[5] source: http://www.lab.anhb.uwa.edu.au/mb140/CorePages/eye/eye.htm

[6] source: http://www.faculty.virginia.edu/rwoclass/astr1230/im/retinal-rods-cones-PE.jpg

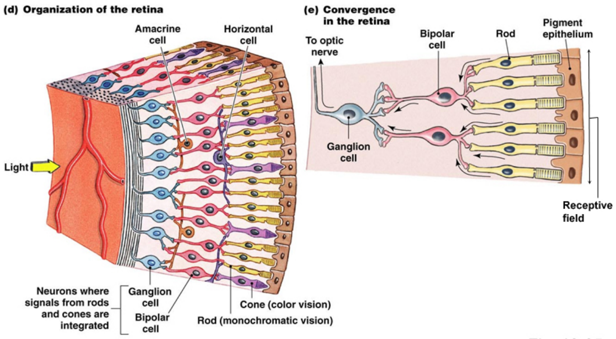

Copyright © 2007 Pearson Education, Inc., publishing as Benjamin Cummings.

Fig. 10-35

Figure 3.4: Human retina

mainly in the peripheral parts of the retina. They are specialized for low light conditions and rod-mediated perception is called scotopic vision. At the twig light, both cones and rods contribute - this is called mesopic vision[12].

Supporting tissues

The main parts of supporting tissue of the eyeball are: sclera (fibrous layer), conjunctiva (transparent thin membrane), and choroid (connective tissue between retina and sclera). The choroid is mainly responsible for the nutritional needs of photoreceptors.

3.2 Cataract

Definition and causes

Cataract is visual impairment caused by progressive opacity in the lens. This condition is very common in elderly and represents the main cause of blindness worldwide[7]. Most common causes of cataract include: diabetes, UV radiation, hypertension, obesity, smoking, previous injury or inflammation, alcoholism, myopia and family history. Rarely, cataract can be a congenital disease, which is characterized by clouding of the natural lens during the intrauterine period[8] .

Signs and symptoms

There are three main types of cataract, which can be diagnosed by examination[13]:

1. Subcapsular cataract with presence of opaque mainly in posterior part of the lens, associated with diabetes

---

[7] source: https://www.who.int/blindness/causes/priority/en/index1.html

[8] source: https://en.wikipedia.org/wiki/Cataract

2. Nuclear cataract with a opaque in the central zone of the lens, associated with advanced age
3. Cortical cataract that occurs in the lens cortex

Symptoms of cataract include blurred vision, progressive loss of vision in one or in both eyes, faded colors, difficulties in the dark and in bright lights. These problems can significantly influence everyday life, but a slow progression of symptoms is most common.

Epidemiology

Prevalence of cataract is much higher in developing world, with 90% of all cases reported globally. According to the WHO published data from 2010, it is estimated that more than 50% of world blindness (around 20 million people) is due to bilateral cataracts[9]. Undeveloped cataract surgery is the main reason for not having appropriate treatment in developing countries. However, with aging population in developed countries the number of cataracts is expecting to grow[14]. The estimated number of performed cataract operations in European Union was 4.5 million in 2016 and varied from 4 to 13 per thousand inhabitants. Austria was on the second place with 13 operations per thousand inhabitants[10].

Prevention of cataract

Cataract may be prevented in some cases using social marketing to reduce smoking, improve protection from UV radiation and provide better control in diabetic patients. However, great majority of cataract patients are relatively healthy people of advanced age. Therefore, surgery is the treatment of choice.

Cataract surgery

Cataract surgery is one of the most frequent surgical procedures performed worldwide. Significant improvement has been made recently in this area of surgery, regarding preparation and evaluation patients before surgery, surgical techniques, equipment, introduction of multifocal intraocular lenses, as well as surgical outcome. Surgical techniques changed during past decades, starting from intracapsular cataract extraction (ICCE), over extracapsular cataract extraction (ECCE) to phacoemulsification. Older techniques included removing the lens, while novel technique uses ultrasound to provide emulsification of the lens[15]. Phacoemulsification has been considered as gold standard for cataract surgery. Small incision, faster recovery and exclusion of regional anesthesia have led to significant improvement in outcomes. Cataract surgery is performed nowadays as a day surgery.

---

[9] source: https://www.who.int/blindness/causes/priority/en/index1.html

[10] source: https://ec.europa.eu/eurostat/web/products-eurostat-news/-/DDN-20190108-1

3.3 Optical Biometry

Definition of optical biometry

Optical biometry is a precise, non-invasive clinical method for calculating intraocular lens (IOL) power [11]. Refractive outcome of all modern surgical methods in cataract surgery with intraocular lens implantation is based on mathematical models of the IOL power calculation.

Ultrasound biometry

Ultrasound biometry represents an outdated method of ophthalmic biometry. It is an invasive procedure which includes contact between cornea and ultrasound probe and therefore carries risk of infection, corneal damage and cause significant pain. Furthermore, examiner should be trained for ultrasound biometry, because accuracy of results depends on appropriate pressure placed on the cornea [16].

IOL Master

History of optical biometry dates back to 1999 when the first optical biometer, called – the IOLMaster was introduced into clinical practice, produced by Carl Zeiss Meditec. IOLMaster biometry is based on partial coherence interferometry, in order to obtain values of axial length (AL), corneal surface curvature, anterior chamber depth (ACD) and visible iris diameter, using infrared laser light. Substantial number of studies showed reliability and accuracy of this device ([4],[5],[6]). Main limitation of the device is failure to provide measurements in eyes with dense leucomas and/or mature cataracts. Improvement in penetration depth can be achieved using an advanced IOLMaster 700 device with addition of a swept-Source OCT measurement.

Optical biometry measurements

Several measurements are included in optical biometry in order to obtain good quality calculations - axial length (AL), keratometry, anterior chamber depth (ACD) and anterior segment biometry.
Axial length (AL) is the distance between anterior corneal surface and pigment epithelium of the retina [17].
Anterior chamber depth (ACD) is the distance between corneal endothelium and anterior lens capsule. According to the literature, inaccuracy in ACD measurement is corresponding with 42% refractive errors following cataract surgery [18].
Keratometry represents the measurement of radius curvature of the cornea. This method includes measurement of the radius of the reflected virtual image,

---

[11] https://cataract-community.zeiss.com/optical-biometry-explained

which is related to the radius of cornea. Further calculation includes conversion of corneal radius to corneal refractive power [19].

3.4 Interferometry

Introduction

Optical interferometry is a technique used for precise measurement of distances, surface irregularities and refractive indexes [12]. A light beam is divided into several beams that travel different paths before recombination. During recombination coherent beams can be added to/subtracted from each other, thus creating an interference pattern.

Michelson interferometer

Optical instruments that create interference are called interferometers. Working principle of an interferometer will be explained using a Michelson interferometer (Figure 3.5): Light wave of a coherent source is split into two paths called a sample arm and a reference arm. Each of the split waves encounters an ideal reflector and is backreflected to the beam splitter, where they are recombined. Difference between the two path lengths (ΔL) produces a phase shift of one of the signals (Equation 3.1, with λ being the wavelength of the light beam). On the other hand, in case of two identical distances travelled by two distinct beams, phase shift will be zero.

$$\Delta\phi = \frac{2\pi}{\lambda}\Delta L \tag{3.1}$$

The detector measures the intensity of the resulting beam, which can be described in proportion to the squares of electrical fields of the reference light beam (E_r) and the sample light beam (E_s) (Equation 3.2)[20].

$$I_o \sim |E_r|^2 + |E_s|^2 + 2E_rE_s cos(2k\Delta L) \tag{3.2}$$

Using a fully coherent light source will result in a phase shift of zero for each phase shift that is a multiple of the source wavelength. For this reason, a technique called low-coherence interferometry or partial-coherence interferometry is introduced for path length calculations.

3.5 Low-Coherence Interferometry

Low-coherent light interferometry results in interference solely when there is no difference in path lengths between the reference and sample arm, bigger than the coherence length of the light used [20]. The coherence length of the source

---

[12] source: https://www.britannica.com/technology/optical-interferometer

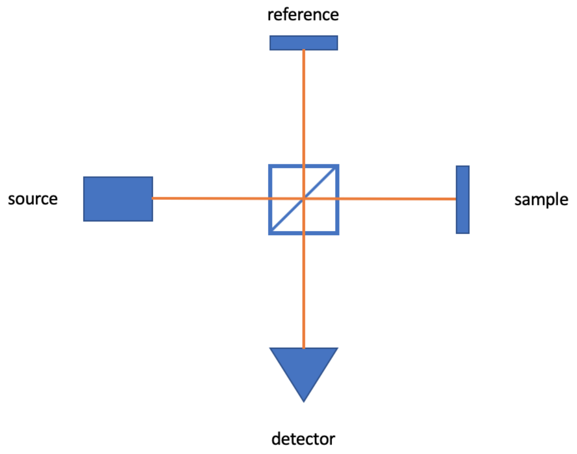

Figure 3.5: Michelson interferometer

can be determined using equation 3.3 [21] (for a Gaussian-shaped light source approximation).
With

- λ_0 - center wavelength of the source ($\lambda_0 = \frac{2\pi}{k_0}$)
- k_0 - central wavenumber
- $\Delta\lambda$ - line width of the source
- Δk - spectral bandwidth defined as Δk=$\frac{\pi}{\sqrt{2ln(2)}}\frac{\Delta\lambda}{\lambda_0^2}$, corresponding to half-width of the spectrum at 1/e of the maximum

$$l_c = \frac{2ln(2)}{\Delta k} = \frac{2ln(2)}{\pi}\frac{\lambda_0^2}{\Delta\lambda} \tag{3.3}$$

Consider a different sample used in a Michelson interferometer setup shown in Figure 3.6, which is not an ideally reflective surface but an object with scattering profile r_s. In contrast, the electric field reflectivity of the reference reflector is known to be r_R.
The light source emits the light with an electric field interpreted by equation 3.4. In this case $s(k,\omega)$ is the amplitude represented as a function of k and ω which represent spacial and temporal periodicities respectively [21].

$$E_i = s(k,\omega)e^{i(kz-\omega t)} \tag{3.4}$$

After entering the beamsplitter, electrical field is divided into two parts E_r for the reference arm, and E_s for the sample arm. The reflected intensities of

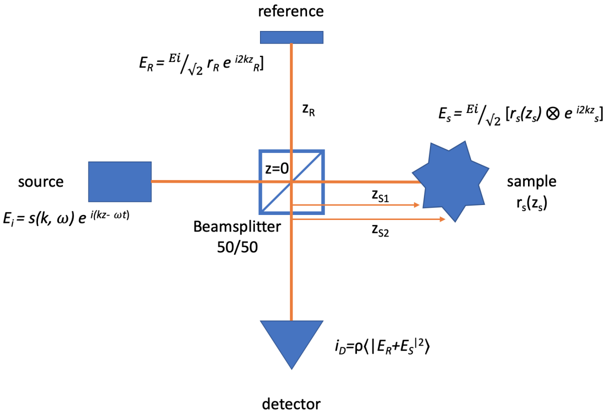

Figure 3.6: Michelson interferometer with a sample with scattering profile r_s

these two are lowered by their respective reflection coefficients (r_r and r_s). With $r_s(z_s) = \sum r_{s_n}\delta(z_s - z_{s_n})$, resulting in electrical fields of the two paths described by equations 3.5 and 3.6 [13]. Note that the factor 2 in the exponent of e-function is attributed to the round trip of the beams.

$$E_r = \frac{E_i}{\sqrt{2}} r_r e^{2kz_r} \tag{3.5}$$

$$E_s = \frac{E_i}{\sqrt{2}} [r_s(z_s) \circledast e^{i2kz_s}] \tag{3.6}$$

After recombination the detector current is described as (3.7) [14]:

$$I_d = \frac{\rho}{2} < |E_r + E_s|^2 > \tag{3.7}$$

Responsivity of the detector is expressed as ρ.

Combining 3.4, 3.5 and 3.6 with the equation for detector current 3.7 and considering that the frequency f (included in angular frequency $\omega = 2\pi f$) is much higher than the response time of the detector, enables the expansion of magnitude squared functions and ensures ω independence of detector current. Finally, by using Euler's simplification temporally invariant equation 3.8 for detector current is obtained:

---

[13] $\circledast$ symbolizes the convolution

[14] $< >$ brackets in equation 3.7 are related to integration over response time

$$
\begin{aligned}
I_d(k) = \frac{\rho}{2}[\frac{1}{2}(R_r + R_{s1} + R_{s1} + ...] \\
+\frac{\rho}{4}[S(k)\sum_{n=1}^{N}\sqrt{R_r R_{s_n}}(e^{i2k(z_R - z_{s_n})} + e^{-i2k(z_R - z_{s_n})})] \\
+\frac{\rho}{4}[S(k)\sum_{n\neq m=1}^{N}\sqrt{R_{s_n} R_{s_m}}(e^{i2k(z_{s_n} - z_{s_m})} + e^{-i2k(z_{s_n} - z_{s_m})})]
\end{aligned}
\tag{3.8}
$$

where R_r, R_s represent power reflectivities of the reflector and the sample. They are determined by magnitude of reflectivities r_r, r_s to the power of two.

Equation 3.8 can be split into three parts (each part represented as a single row). The first part is a so called "DC term" that has a constant value and is not influenced by the change in path distances. The second part is called "cross-correlation" and it provides information about the path length inequality between sample and reference arm, which is essential for interferometry. The third part is called "auto-correlation" and it provides information about the differences in distinct parts within the same path.

To conclude, the cross-correlation part of the equation 3.8 is where the relevant information for low coherence interferometry is hidden. The intensity in the cross correlation can be described by equation 3.9. Therefore, by varying k or z the information about the mismatch in path lengths can be acquired. According to which of the two variables is fixed and which can be altered, low coherence interferometry is characterized as "Time-domain" LCI (when varying z) or "Fourier-domain" LCI (when varying k).

$$
I(k, \Delta z) \propto cos(2k\Delta z) \tag{3.9}
$$

Fourier-domain LCI can further be divided into spectral-domain and swept-source LCI. For performing biometry, it is best to use swept-source LCI because of its high sensitivity and larger coherence length.

3.6 Wavelength-Swept Lasers

Wavelength swept lasers are characterized by the fact that their wavelength can be varied over time called "tuning" [22].

Tuning

Typically, spectrum/wavelength profile of a swept-source laser resembles a Gaussian curve (Figure 3.7).

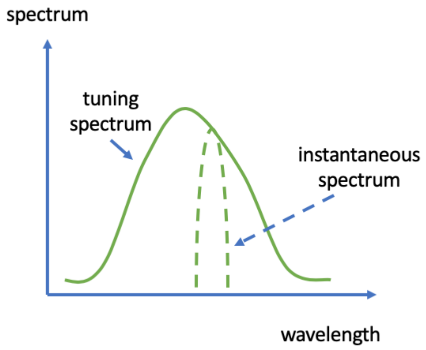

Figure 3.7: Swept-source laser: tuning spectrum

Tuning range $\Delta\lambda$ is per definition measured from edge to edge of the tuning spectrum at $-3dB$ or at $1/e^2$ level [22].
For the use in interferometry, it is the wavenumber k needs to be tuned linearly. These two variables are related by $k = 2\pi/\lambda$. Linear tuning of k leads to uniformity in sampling the interference signal [22]. Unfortunately, as a rule, wavenumber tuning is mostly non-linear. Therefore, remapping of the data needs to be performed in post processing.

Axial resolution

As described above, the axial resolution (3.10) of a laser source is dependent on the coherence length of the light source [20] and is therefore expressed as:

$$\delta z = \frac{2ln(2)}{\pi}\frac{\lambda_0^2}{\Delta\lambda} \tag{3.10}$$

with λ_0 representing center wavelength of the source, and $\Delta\lambda$ its tuning range (bandwidth).

For performing eye measurements, the optimal center wavelength λ_0 is either 850 nm or 1060 nm, because of the local minimums of light absorption in water in the infrared region (Figure 3.8)[15]. Infrared light is used due to its large penetration depth and is more pleasant for the patients.

---

[15] source: https://omic.ogi.edu/spectra/water/data/hale73.dat)

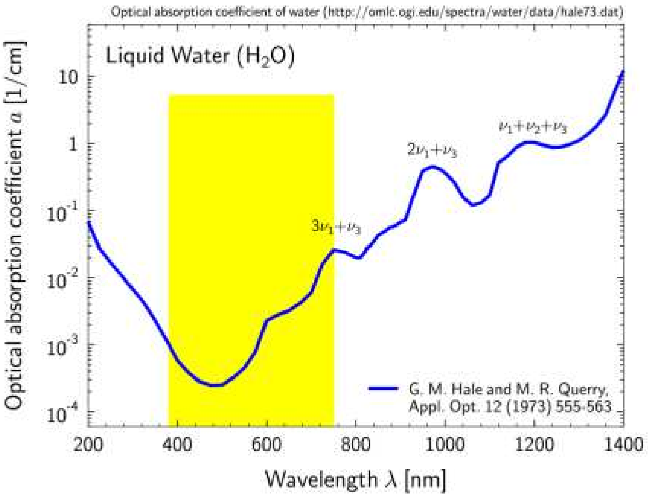

Figure 3.8: Light absorption in water

3.7 Vertical-Cavity Surface-Emitting Laser

Edge-emitting vs. Surface-emitting lasers

In order to get a better understanding of how the vertical-cavity surface-emitting lasers (VCSELs) work, one must first get familiar with theory of operation of conventional edge-emitting lasers. They are characterized by a typical double heterostructure, which is used both as a limits of the active region and as a waveguide for the laser beam.[16] The wave is then directed to exit perpendicular to the layered structure (by the resonator) and produces an elliptical astigmatic and asymmetric diverging laser beam.

Optical cavity orientation in vertical-cavity surface-emitting laser diodes however, is orthogonal to the one found in edge-emitting laser diodes[23]. Surprisingly, this difference in spatial configuration of the laser diode affects the resulting beam characteristics, scalability design, production etc.

Structure of a VCSEL

Every laser by definition has three main components:

- Energy pump
- Active medium
- Optical resonator (Reflectors)

---

[16] source: https://www.rp-photonics.com/edge_emitting_semiconductor_lasers

VCSELs use the inflow of current as the energy source. Active region is formed by a number of very thinly layered quantum wells, whereas the reflectors are multi-layered Bragg gratings, which are wavelength-selective mirrors [24]. The explained structure is depicted in Figure 3.9.[17]

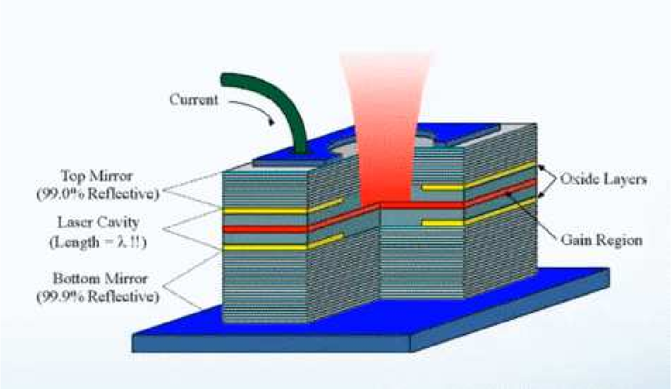

Figure 3.9: VCSEL structure

Typical output of a VCSEL is a circularly symmetric diverging Gaussian beam. Usually, the wavelength of the resulting beam is dependant on the materials in use, structure, dimensions etc. However, tuning of the VCSEL provides control over the output wavelength. Tuning can be performed thermally and electrically, with slow thermal tuning producing larger tuning range values (wavelength range). However, in case of high tuning speeds, such is the case in low-coherence interferometry, electrical tuning provides better results.

Electrically pumped VCSEL

Tuning of a laser diode can be done thermally, optically or electrically (by carrier injection). Electrically pumped VCSELs achieve a change in wavelength with varying electrical current. The advantage of an electrically pumped VCSEL, in comparison with the thermally tuned one, is that it can be used in higher speeds, since, there is no need for an inactive "cool-down" period. However, some undesirable heating does happen in an a current-tuned VCSEL as a result of the current flow through the materials above and under the DBR mirror systems [25].

Applications and Advantages

Numerous advantages including low power operation, circularly symmetric high-quality optical beam, potentially low cost manufacturing, ease of optical fiber coupling etc. account for the research done on them in the last few decades.[26]

---

[17] source: https://www.ametek-ecp.com/resources/blog/2019/february/what-is-a-vcsel

Due to their numerous benefits, VCSELs have a wide variety of applications in different fields [18]. Some of them include:

- Differential absorption sensors (e.g. blood gas),
- Photoelectrics
- Light guide illumination
- Hand-held optical ranging
- Air data links
- Atomic clocks
- High-precision encoders
- Speckle-based sensors
- Interference Sensors

3.8 Photodiode

Definition

A photodiode is a semiconductor electrical component manufactured in a way that the incident light can arrive at the junction region. In most cases it is either a silicon or germanium junction diode [27]. Basically, it converts radiation into electric current. Photodiodes have many advantages [19], including quite good linearity, low noise, long life etc.

Working principle

The energy provided by incident light creates leads to the crossing of a valence electron to the conduction band. This is followed by an increase of the current, but much more effectively in reverse-biased mode [20].

3.9 Instrumentation Amplifier

Theory and application

Precise electronic measurements of a difference between two signals call for high common mode rejection ration and prospective amplification of the useful part

---

[18] source: https://www.finisar.com/sites/default/files/resources/an-2140_vcsels_in_various_sensor_applications_finisar.pdf

[19] https://www.elprocus.com/photodiode-working-principle-applications/

[20] source: "Elektronische Messtechnik" Lecture Slides by Prof. Martin Gröschl (Version 1.2)

of the input signals [28]. Instrumentation amplifier is an integrated circuit with characteristically high gain, very large input impedance and high CMRR built for this purpose.

Working principle

Circuit consists of two parts (shown in Figure 3.10) : two non-inverting operational amplifier circuits followed by a differential amplifier circuit.

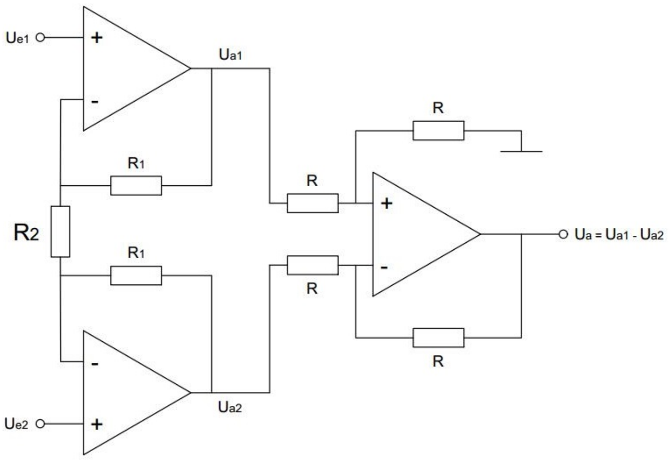

Figure 3.10: Instrumentation amplifier circuit

In the first part of the circuit, it is of high importance to match the resistor values. Otherwise, the CMRR will be compromised.
The second part is a differential amplifier circuit. Output voltage of the differential amplifier circuit is explained by Equation 3.11.

$$U_a = U_{a1} - U_{a2} \tag{3.11}$$

Gain calculation

Gain of the whole circuit can be calculated with the help of a voltage divider circuit shown in Figure 3.11. Exact steps for its derivation are demonstrated by Equations 3.12 and 3.13.[21]

$$\frac{U_{a1}}{U_{e1}} = \frac{R_1 + R_2/2}{R_2/2} = \frac{2R_1 + R_2}{R_2} = \frac{U_{a2}}{U_{e2}} \tag{3.12}$$

$$\frac{U_{a1} - U_{a2}}{U_{e1} - U_{e2}} = \frac{U_a}{U_{e1} - U_{e2}} = 1 + \frac{2R_1}{R_2} \tag{3.13}$$

---

[21] source: "Elektronische Messtechnik" Lecture Slides by Prof. Martin Gröschl (Version 1.2)

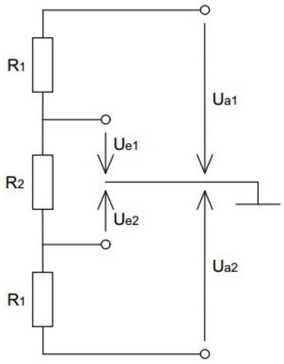

Figure 3.11: Voltage divider

This means that the total gain of the circuit can be controlled by appropriate selection of the resistor R_2, which is why this resistor can be controlled externally.

3.10 Parallel Analog/Digital Converter

Introduction

Parallel ADC (also Flash ADC, direct conversion ADC) is built by creating a "linear voltage ladder" connected by a number of comparators to measure. Each comparator compares the input voltage to a distinct reference voltage. (Figure 3.12) Finally, digital encoders are connected to the comparators creating digital outputs with two comparator circuits needed for generation of 1 bit [28].

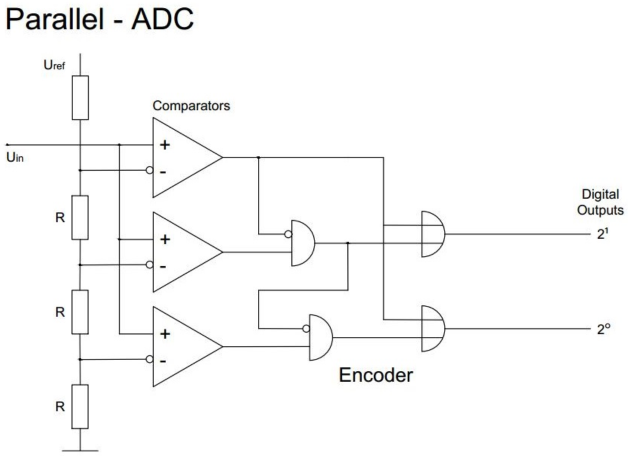

Figure 3.12: Flash ADC

Working principle

Each comparator circuit determines whether the input voltage (U_{ein}) is larger than the reference voltage (which is different for each comparator due to the voltage dividers). Every flash ADC consists of $(2^N - 1)$ comparators, where N represents the number of bits.

Advantages/Disadvantages

The biggest advantage of a parallel ADC is the conversion speed, which is higher than in any other ADC type. However, there are many drawbacks to this circuit as well, e.g. the large number of comparators needed implies larger costs and size and also higher power consumption.

Chapter 4

Setup

4.1 Optical System Setup

Current system setup including a fiber setup and a free propagation setup created by Dr Ferrara is shown in Figure 4.1 [1] Switching between the two setups is achieved simply by flipping a mirror. To begin with, we will get acquainted with the working methods of both these setups.
The working principle of the system of the free propagation system is as follows: In the beginning,VCSEL beam is collimated with an initial lens. The collimated beam then passes through a $\lambda/4$ waveplate, which changes the linear polarization of the VCSEL into an circular one. It follows to a polarizing beamsplitter (PBS) that divides the beam in two components, accordingly with the elliptical proportions. The part of the beam with polarization "s" is deflected at 90° (sample arm) and the part with polarization "p" is transmitted (reference arm). By changing the orientation of the quarter wave plate at the entrance, the power between sample arm and reference arm is divided (ratio from 50/50 to 100/0). This is done to control the power transmitted to the patient's eye and ensure the safety of the patient.
The sample arm beam travels through an additional $\lambda/2$ plate. This wave plate is used to ascertain that the beam that exits the polarizing beam splitter has the same polarization as the wave that returns to the polarizing beam splitter after being reflected by the sample (which should maximize the light detection).
The reference arm beam goes through a neutral density filter that reduces the power of the beam since too much power on the reference arm results in increased general noise and may saturate the detector.
Finally, a non-polarizing beam splitter is used to recombine the reference and sample beam and interference happens. The interferometric signal can be described by a sinusoidal wave, the frequency of which depends on the mismatch dz between the sample and the reference arm (Equation 4.1, see also equation

---

[1] This Figure as well as information about the setup in Chapter 4 are the courtesy of Dr Lorenzo Ferrara for whose setup the low-cost electronic solutions in this thesis will be made.

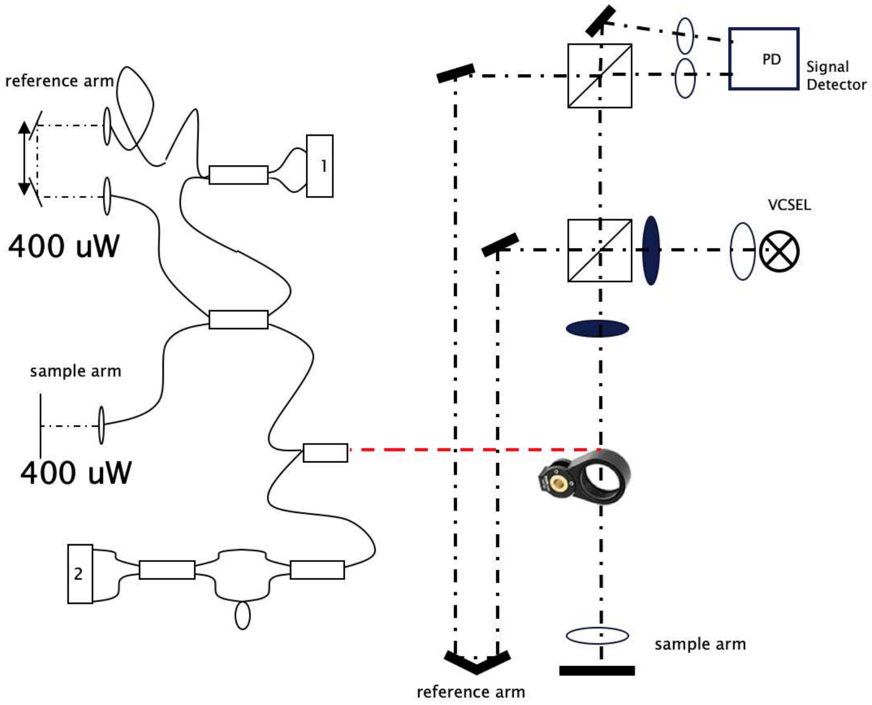

Figure 4.1: Current System Setup: Fiber- and Free propagation system

3.9.

$$y = cos(2(k_0dz) \tag{4.1}$$

The resulting beam, containing the interferometric information is split into two equal beams that are then focused onto a dual balanced detector (Thorlabs PDB450A-AC). This detector only collects the interferometric spectrum and this information is then sent to a personal computer. The fiber-coupled setup, on the other hand, has a slightly different working principle:
After the flip mirror, a small portion of the beam (around 5%) is sent to a Mach-Zenhnder interferometer (Thorlabs INT-MZI-850), that uses the interference information of the entering beam (creating a time delay) to later provide data for non-linearities reconstruction. The rest of the beam is then divided in two equal parts for reference/sample arm by a fiber coupler. After hitting the sample(eye)/mirror in case of sample and reference arms respectively, the reflected beams are then recombined in a 50% beam splitter. The resulting wave then enters a balanced detector (Thorlabs PDB450A-AC), as it was the case with the free propagation setup.
The two different setups both have their advantages. Free propagation setup

provides more power on the sample, whereas the fiber coupled setup requires less space which makes it more suitable for a compact portable device. In addition, fiber coupled setup results in a better reconstruction, probably because the enclosed waves should be less exposed to external noise in general (in comparison with waves in free propagation setup).

4.2 System Electronics

4.2.1 Source

As previously mentioned, the source of a laser is a Vertical-Cavity surface-emitting laser diode (VCSEL). The VCSEL is electrically driven by a laser driver (Newport model 500), which provides a DC current of 8mA. This current corresponds to an optical power of the laser of aproximatelly 2mW. The external current modulation is provided by connecting a waveform generator (Agilent 33220A) to the Newport laser driver. Modulation signal is a triangle wave with duty cycle of 50%. One sweep is the equivalent of one up or one down ramp. Should we acquire over both ramps (up and down), we would obtain two almost identical signals but the differences would result in noise and the measurement would be less precise, since less sample points per ramp would be used. The modulation frequency has to be high enough to secure fast measurements in order to minimize motion artefacts. On the other hand, the value cannot be too high (like eg. 100kHz), since the VCSEL would fail to follow the modulation speed, and the sensitivity would be lost (reduced integration time causes less photons to arrive on the detector). Hence, the used value of the modulation frequency is 2KHz. The waveform generator is used in burst mode with 1 single burst, meaning that with every trigger a single ramp is obtained. Triggering is used to synchronise signal acquisition exactly when the sweep begins. The FPGA controls the trigger (square signal, 2kHz, up sweep of 20 μs) and sends signals to the function generator and to the acquisition card.

4.2.2 Detector

On the detector side, a balanced detector (Thorlabs PDB450A-AC) and a reference interferometer (Thorlabs INT-MZI-850) are used. Data from these two components are transmitted to a data acquisition board (Alazartech ATS9870) that is implemented into a PC. As already mentioned, the acquisition is synchronised via the FPGA.

4.2.3 Overview

As shown in Figure 4.2, financial resources spent solely on this setup are approximately 4700 €. This number does not include the triggering or the acquisition costs (FPGA or the acquisition board).

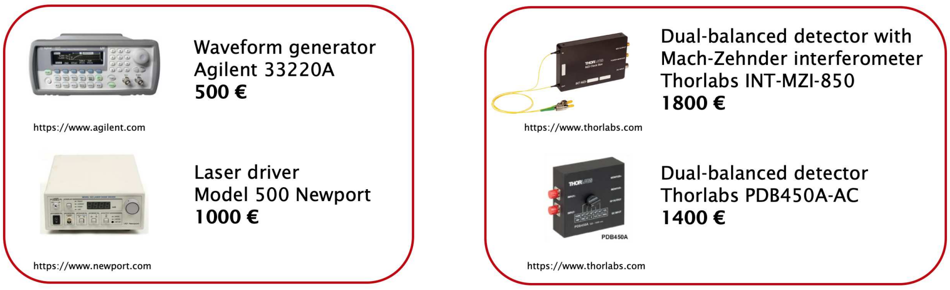

Part I: Source

Part II: Detector

Figure 4.2: Initial costs of system electronics

Chapter 5

Methodology

5.1 Source

Firstly, a fitting vertical-cavity surface-emitting laser diode is to be chosen. Eye measurements are usually done in infrared range. Which wavelength is emitted by the VCSEL laser is dependant on the material. Furthermore, the water absorption should be taken into consideration, which limits the choice to two options in IR region: 850 nm or 1060 nm. It was decided to use a 850 nm single mode VCSEL because of the wider variety of choices at this wavelength, as it is also widely used in telecommunications. Apart from that, the tuning range of the laser diode should be as large as possible.

5.1.1 VCSEL Characterization

Method for VCSEL characterization is shown in Figure 5.1. Firstly, the exit beam of the VCSEL source in test is collimated using a collimator lens. The beam then encounters a fiber collimator before entering into a spectrometer.

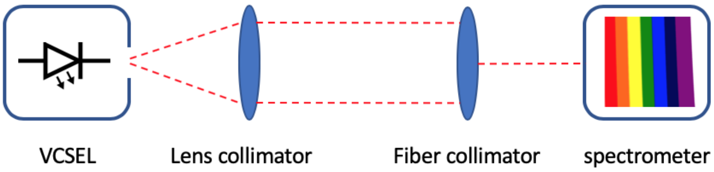

Figure 5.1: Methods: VCSEL characterization

The results can be displayed either as a wavelength over time graph, with the tuning range of a VCSEL measured from lowest to highest λ value, or as a spectrum intensity over wavelength graph (Figure 5.2). In this case instantaneous spectra for discrete wavelengths can be seen, as well as the envelope function, representing the tuning spectrum. Tuning range is determined from the graph as the width of the envelope at Full-width half-maximum (FWHM), also called spectral bandwidth.

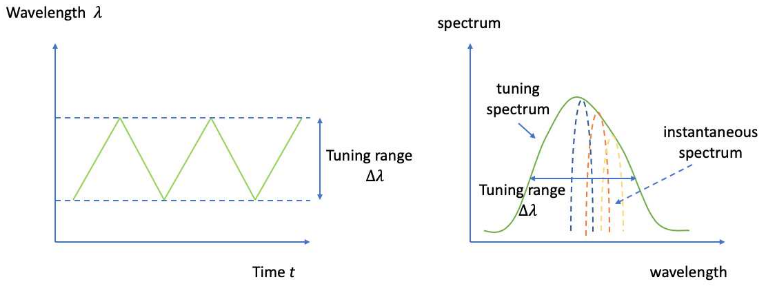

Figure 5.2: VCSEL characterization: displaying results

5.1.2 Managing Source Non-linearities

In biometry, failure to eliminate source non-linearities in wavelength tuning results in the broad spikes in the Fourier analysis of the backscattered light from parts of the eye (retina, cornea, eye lens). In consequence, the exact position of the eye components is not precise, causing even bigger problems with determining the distance between them.

The chirped signal can be relinearized using the information of the phase ramp of a mirror interference signal or using the reference interferometer. In order to perform the relinearization following steps must be performed:

1. Obtain a spectrum of the chirped signal.
2. Extract the phase.

   Phase extraction is performed as follows: Real part of the signal undergoes a Hilbert transformation in order to get the analytical complex signal. This Hilbert transformed signal is then used to obtain its real and imaginary parts respectively. Phase is calculated using equation Phase $= arctg(\frac{real}{imaginary})$. Lastly, the phase needs to be unwrapped because it is periodical (pi to π range).

3. Remap the signal with information of its phase, using linear interpolation.
4. Relinearize the signal.

The original signal is remapped using interpolation.

5.1.3 Current Driving

After deciding on the laser source, different economically available options for current driving of the laser diode in question are to be explored. This was followed by testing their suitability for the task by determining the tunability of a VCSEL with a certain laser driver using VCSEL characterization method. Comparing the tuning ranges achievable with each laser driver should determine which one has a better tuning performance, see 5.3. In addition, it has to be analyzed what current interval is used to achieve the tuning of a VCSEL. Large intervals lead to increased power consumption.

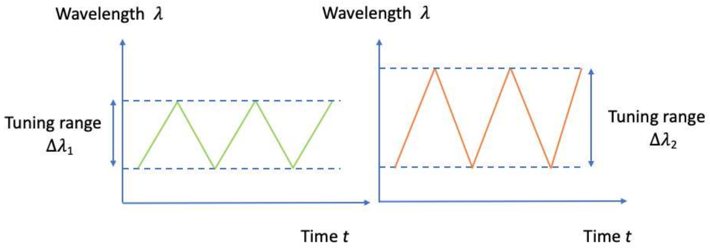

Figure 5.3: Methods: comparing two laser drivers, based on VCSEL tuning range

5.2 Balanced Detector

There are be two main parts to consider when designing a balanced detector circuit. Firstly, one must choose an appropriate detector diode with a fitting central wavelength of maximum sensitivity (¿90% ideally). Secondly, one must choose a differential amplifier fast enough to follow the change in high-speed input signals and a highest possible common mode rejection ratio to avoid noise amplification. The output signal of the resulting circuit should be a voltage difference between the two photodiodes, ready to be digitized for further post-processing.

5.2.1 Photodetector diodes

The output of a typical photodetector diode is measured as a current, rather than voltage, which is why most balanced detectors need a transimpendance amplifier before entering a differential amplifier. However, this scenario makes the circuit more noise sensitive due to amplification (not true in case of an integrated circuit). For this reason, it would be wise for a photodiode with integrated amplifier. Furthermore, it is important that the circuit is achieved without a Schmitt trigger. Since the circuit has a voltage threshold for switching states, it can happen that the signal cannot exceed the threshold, thus leading to information losses.

5.2.2 Circuit design

Some of the main concerns when choosing the adequate components for the balanced detector were noise reduction and low change in bandwidth with increasing gain. After careful consideration, two instrumentation amplifiers were chosen for two experimental designs:

- **Version 1:** a circuit built around the instrumentation amplifier **AD8221**
- **Version 2:** a circuit built around the instrumentation amplifier **AD8253**

Circuit Version 1

Instrumentation amplifier AD8221 by Analog Devices is a precision instrumentation amplifier that claims to provide the highest Common - Mode - Rejection - Ratio over frequency on the market.[1] Another plus was a wide range of gain values, controlled by choosing an appropriate resistor. Its applications include precision data acquisition systems as well as medical instrumentation, which sounds promising. Price of AD8221 according to Digikey.de is less than 6 €.

Even though the instrumentation amplifier has a large input impedance, which should minimize the influence of noise, bypass capacitors should be introduced into the circuit. A ceramic capacitor of 100nF and a tantalum electrolytic capacitor of 10μF should be placed near the power supply pins to reduce any noise introduced by the prospective AC components.

Circuit Version 2

Instrumentation amplifier AD8253 by Analog Devices is an instrumentation amplifier that is characterized by a very high input impedance (counted in GΩ according to its datasheet), which has a digitally programmable gain. It belongs to a group of high speed amplifiers, and has a bandwidth as high as 10MHz (when Gain is equal to one), and that theoretically makes it a suitable choice for our application. Additionally, datasheet of AD8253 states biomedical analysis, data acquisition and test and measurement as common applications, all of which are needed in this project.[2] Similarly to AD8221, this amplifier costs about 6 €

---

[1] Datasheet: https://www.analog.com/media/en/technical-documentation/data-sheets/AD8221.pdf

[2] Datasheet: https://www.analog.com/media/en/technical-documentation/data-sheets/AD8253.pdf

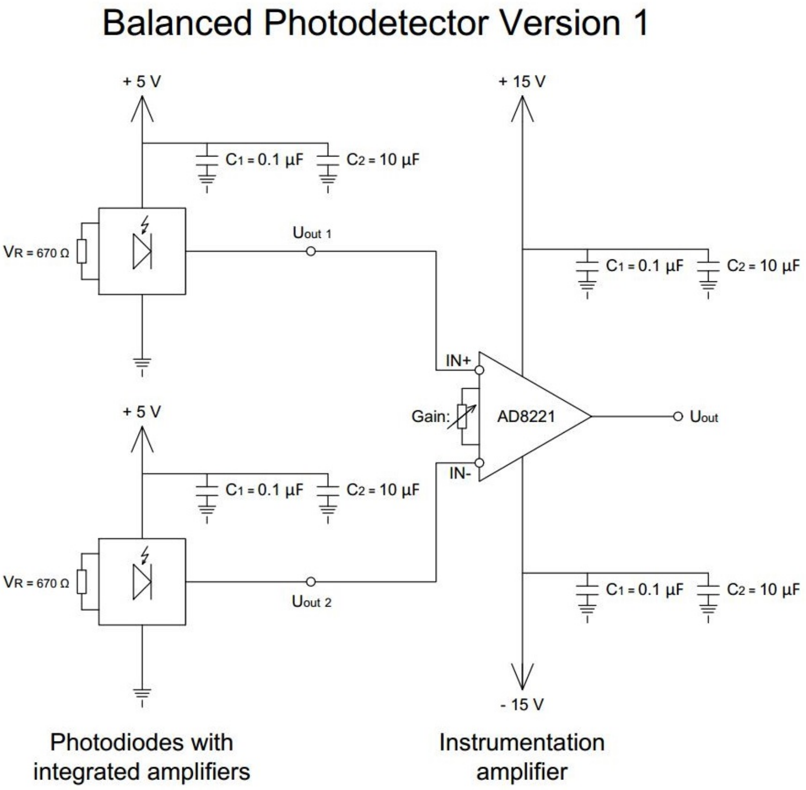

Figure 5.4: Balanced Detector: Circuit version 1

(according to Digikey.de).

As previously mentioned, gain of the amplifier circuit is digitally programmable using the Table 5.1:

Gain: Truth Table Logic Levels			
WR	**A1**	**A0**	**Gain**
-V_s	Low	Low	1
-V_s	Low	High	10
-V_s	High	Low	100
-V_s	High	High	1000

Table 5.1: Digitally programmable gain: truth table

Besides the change in instrumentation amplifier and a different gain settings, not much was modified in comparison to circuit version 1. Noise handling, for example, was done in the same manner.

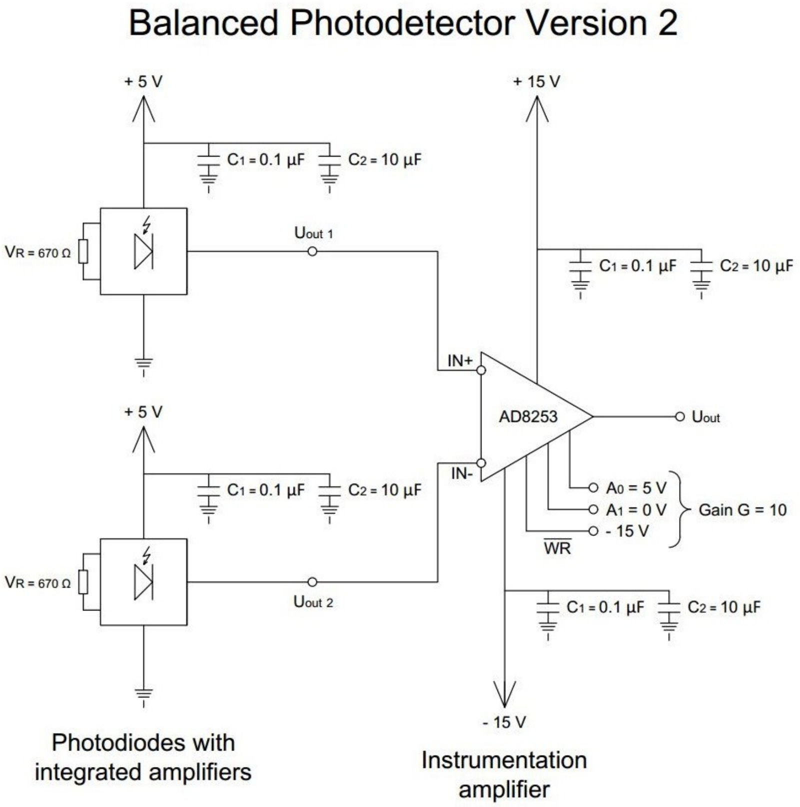

Figure 5.5: Balanced Detector: Circuit version 2

Prototype 1

The first prototype is assumed to be used only as a proof of concept and should therefore be built on a breadboard (Figure 5.6). Since the photodiodes are supposed to be used as surface-mount components, thin wires have to be soldered onto them. This complicates the measurements because of contact losses between the wires of inadequate size and the breadboard. Another great disadvantage of this prototype is the inconvenient mounting of the optical fibers from the optical setup onto the small light sensing area of the detector, as suspected. Namely, the laser beam (invisible to naked eye) is to be aimed at an area of 0.4 x 0.35mm. These potential problems encouraged the design of the second prototype.

Prototype 2

As the mounting of the optical fibers onto the photodetector diodes could possibly be a challenge for test performance, a 3D CAD model of a potential mount was designed and printed out on a 3D printer. Design of the prototype 2 is

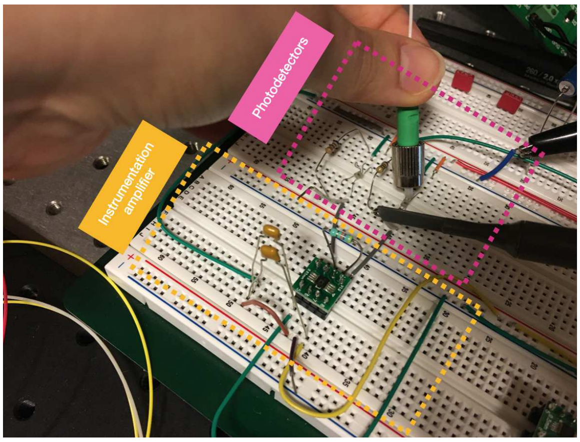

Figure 5.6: Prototype 1: Breadboard

shown in Figure 5.7. Photodetectors are soldered onto a small experimental stripboard, while the rest of the circuit (mentioned in prototype 1) stays on the breadboard to ease the switching between the circuit with instrumentation amplifier AD8221 and the circuit with instrumentation amplifier AD8253.

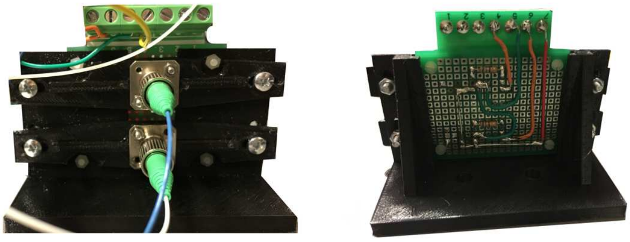

Figure 5.7: Prototype 2: Mount for the fiber setup

Prototype 3

Prototype Nr.3 is supposed to be designed as a printed circuit board, with the goal of potentially improving the overall design and performance of the detector. This would both solve the problems with surface-mount diode connections, as well as lower the noise in general. Keeping in mind that the third prototype would, ideally, be implanted into the existing optical system permanently, we must provide a solution with a single power supply and a housing for the detector circuit. The circuit designs (version 1 and 2), according to which the PCB will be designed, is shown in Figures 5.8 and 5.9. Note that the bypass capacitors placed near any supply pins are not shown in these circuits, but will be a part of the final PCB.

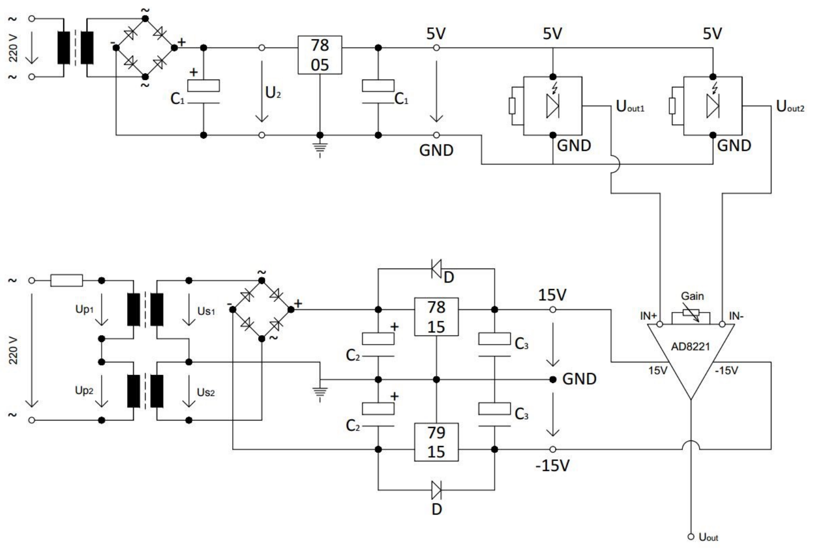

Figure 5.8: Balanced Detector: Prototype 3, version 1

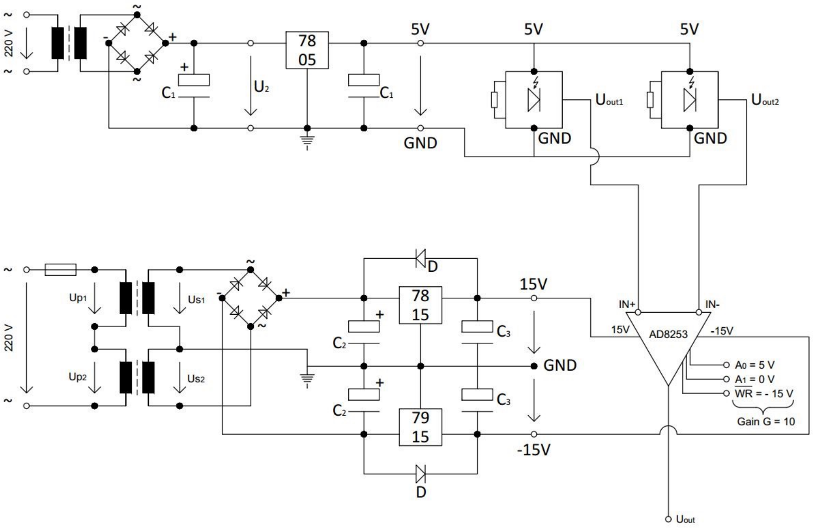

Figure 5.9: Balanced Detector: Prototype 3, version 2

5.3 Compact System

The original idea was to make a compact system that would consist of the optical system and electronics. Electronics would be controlled by a Raspberry Pi microcomputer board that would be connected to the source via DAC followed by a laser driver on one hand, and to the detector via ADC on the other hand. This concept would also allow easy implementation of an LCD screen provided that it was needed for system control in the future.

5.3.1 Controller Board Choice

Instead of using a high speed microcontroller, Raspberry Pi 3B+ was chosen for the task of running and controlling the prospective compact system. This was done due to the need for independent tasks that are to be run simultaneously, which is not an option for any microcontroller. Hypothetically, this microcomputer should offer all the advantages of a personal computer for a price of approximately 37 € (according to conrad.at). Furthermore, a Raspberry Pi board offers the possibility of adding a monitor and a keyboard to the system, which can prove useful for user-friendly application of the end product.

5.3.2 AD Conversion (used with the balanced detector)

In order to process the analog data obtained by the balanced detector, it needs to be digitized using an analog-digital converter (ADC). The choice of the ADC to be used for this setup was influenced by the speed of the data acquisition. Namely, it had to be able to work at speeds over 10 Msps. For this reason, a parallel ADC is the most suitable option, because its structure (each bit having its own path and output pin) allows for the a low conversion time.

5.3.3 DA Conversion (used in current driving)

Unlike the speed limitations in the choice of an ADC, the frequency used in current driving is expected to be no more than 2kHz. For this almost reason any DAC would suffice in terms of conversion speed. The choice was then influenced by the ease of connection with a raspberry Pi board.

Chapter 6

Results

6.1 Source

6.1.1 VCSEL characterization

VCSELs from two manufacturers were characterized using a spectrometer in order to choose the one with the largest tuning range.
Sweep spectra at the Frequencies of 1Hz, 100Hz and 2kHz of a Phillips single mode VCSEL ULM850-SingleMode-B2-PL are shown in Figure 6.1. On the fourth graph the envelope is depicted, allowing an easier determination of the tuning range. It can be seen from the spectra that the tuning range of this VCSEL lowers from approx. 12nm at 1Hz to approx. 9nm tuning range at 2kHz, which will essentially be the frequency to use for the biometric measurements of the system.

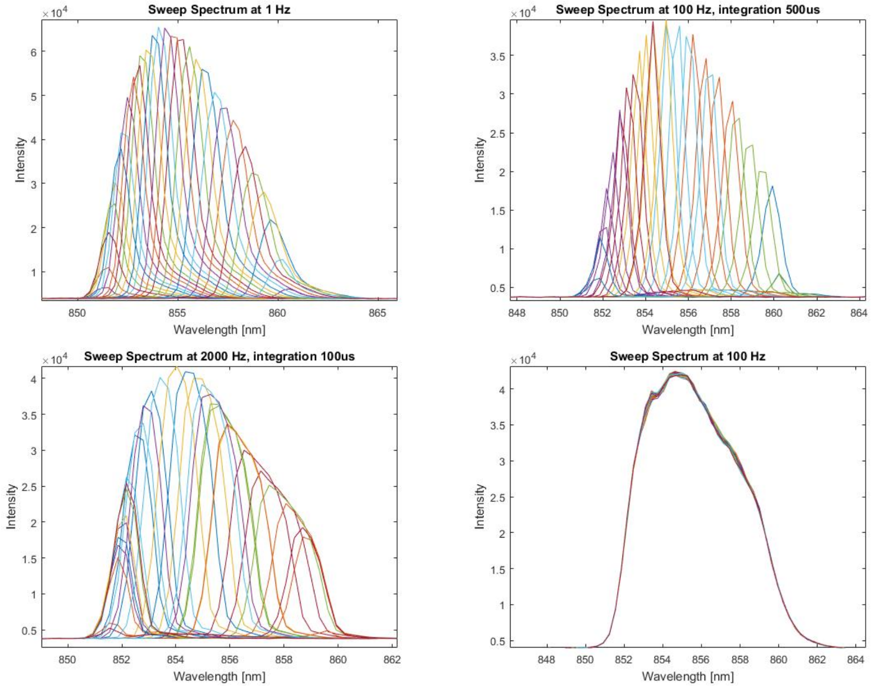

Figure 6.1: Phillips VCSEL Spectra

Following the sweep spectra of two Frankfurt single mode VCSELs FU-850-2.0-POL-TO46 (Figure 6.2)are shown. Contrary to the graphs of the Philips VCSEL spectra, that show Gaussian-looking curves, Frankfurt VCSEL spectra seem to be distorted, even at low frequencies (especially in graphs 4 and 5). These disturbances could indicate different modes in the laser beam coming out of the VCSEL. Furthermore, as previously mentioned, two VCSELs of the Frankfurt kind were tested (first one: graphs 1-3, second: graphs 4-5 in Figure 6.2) and there are clear inconsistencies in the spectra between the two laser diodes from of the same kind. Therefore the VCSEL of choice was the Phillips one.

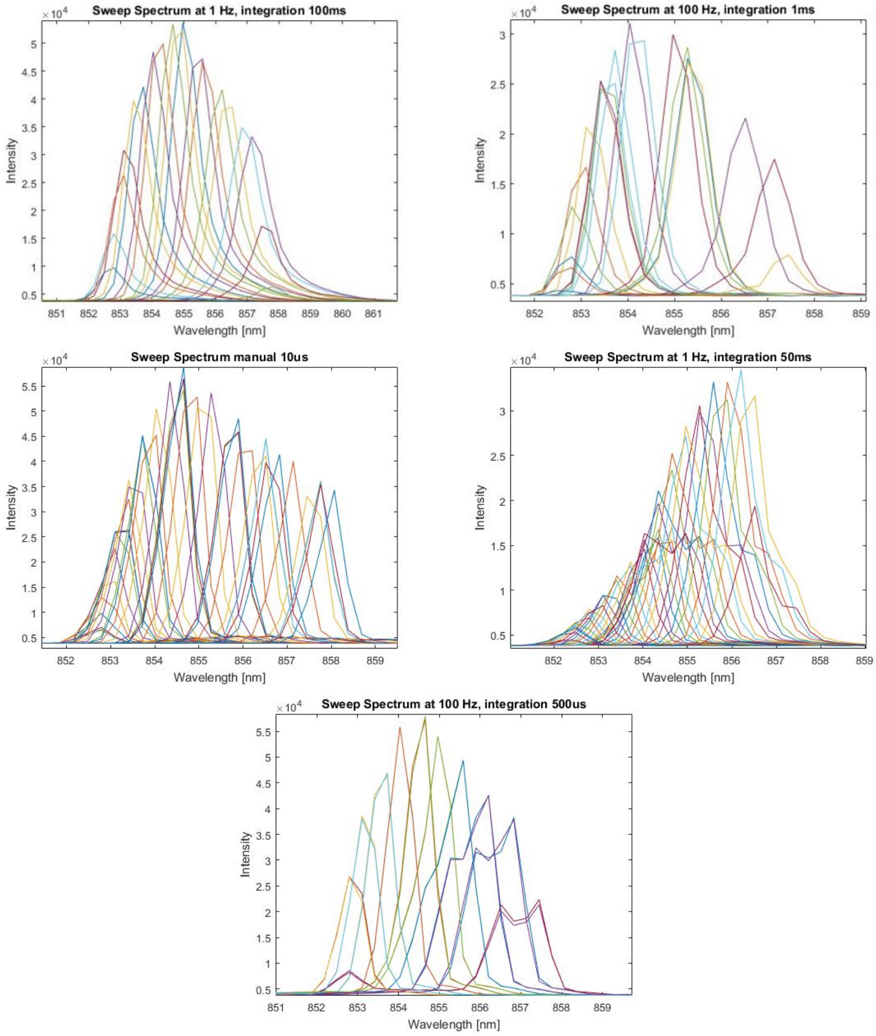
Sweep Spectrum at 1 Hz, integration 100ms
Sweep Spectrum at 100 Hz, integration 1ms
Sweep Spectrum manual 10us
Sweep Spectrum at 1 Hz, integration 50ms
Sweep Spectrum at 100 Hz, integration 500us

Figure 6.2: Frankfurt VCSEL Spectra

6.1.2 Current driving

In figure 6.3 you can see the Analog Technologies' low noise constant current laser controller ATLS100MA103 with the corresponding evaluation board.
This electronic module was chosen due to its ability to generate a constant output current, as well as perform current modulation, controlled externally by a waveform generator. Furthermore, it offers the ability to set the output current limitation, by choosing an appropriate potentiometer resistance value. However, it is advisable to build a custom circuit for the laser driver, since the tests have shown that the evaluation board keeps giving out the current at the last saved amplitude, when the external modulation is turned off. Also, current limitation only shuts down the board for a small period of time, which can still

Figure 6.3: Low Noise Constant Current Laser Controller ATLS100MA103

lead to burning of a VCSEL at high modulation frequencies.

Current drivers: Analog Technologies vs. Newport

In order to test the performance of the Analog Technologies laser driver electronic module in comparison to the Newport driver (currently used in the setup), a spectrometer was used. Tests were performed with modulation frequency of 2kHZ and duty cycle of 50%, which are the values to use for the biometry measurements with this setup. The results are shown in Figure 6.4, with time on the x-axis and wavelength on the y-axis. As we can clearly see, both the Newport driver and the low-cost current driver by Analog Technologies, achieved the same VCSEL tuning range of 8.5 nm.

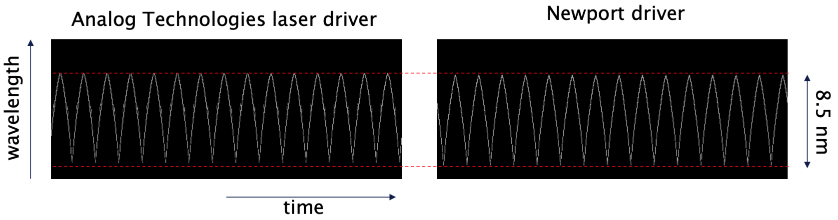

Figure 6.4: Current driving: Analog technologies vs. Newport

A more interesting fact, not visible in the previous figure is the result of the power consumption of both drivers (Table 6.1). Surprisingly, diode laser driver by Analog Technologies consumed much less power for the same task, meaning that the same VCSEL tuning range was reached with only a portion of the power consumption of the original driver used in the setup.

Current driver comparison: modulation properties			
	Current offset	**Modulation voltage**	ΔV
Analog Technologies	$0\ mA$	30 to $220\ mV$	$190\ mV$
Newport	$8\ mA$	-500 to $940\ mV$	$1440\ mV$

Table 6.1: Current drivers: Modulation properties comparison

6.1.3 Current- vs. Phase-based relinearization

Method for signal relinearization is performed by extracting $Phase/k$ information from the chirped signal and doing an interpolation to obtain a relinearized function. Reffering to the equation 6.1, the information about k is required. This information is not easily recovered.

$$I(k, \Delta z) \propto cos(2k\Delta z) \tag{6.1}$$

The information on t however, is simple to acquire. Our hypothesis is that current vs. time (i/t) dependency can be related to phase vs. wavenumber $(Phase/k)$ dependency. To put this hypothesis to the test, the i/t information was obtained by monitoring the current output of the laser-driver evaluation board, whereas the $Phase/k$ information was extracted from the spectrum.

The steps for relinearization were changed in order to fit the current information:

1. Obtain a spectrum of the chirped signal
2. Extract the averaged current information

   When monitoring the current, a modulation is recorded every 500μs, meaning that not only one graph is obtained but a thousand. These are used for finding irregularities that could indicate e.g. motion artefacts. In order to suppress noise, these graphs are averaged.

3. Extract the phase for comparison. Proceed only if phase and current graphs are similar.
4. Remap the signal with the information from the current using interpolation.
5. Relinearize the signal.

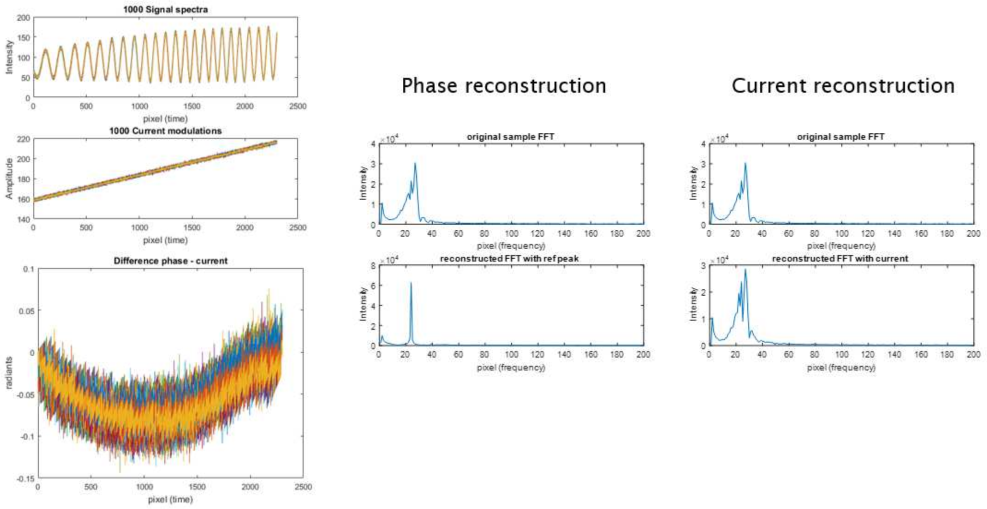

Figure 6.5: Results: Phase vs. Current reconstruction

The obtained results are shown in Figure 6.5. It is noticeable from the graphs that the large differences between the $Phase/k$ and i/t led to an unsatisfactory outcome for current-based relinearization of the peak (on the right), compared with commonly used phase-based relinearization.

6.2 Balanced Detector

6.2.1 Photodiode

It was decided to use Panasonic PNA4U73F photodiode with integrated amplifier (Figure 6.6). The cost of a single piece comes to 0.135 € according to RS components. As potentially problematic we can label the dimensions of the detector, with only 2.8 x 2.4 x 1.4 mm, and the light sensing detector area of

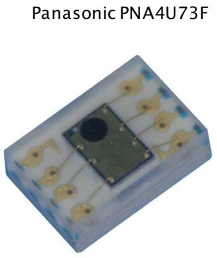

Figure 6.6: Photodiode Panasonic PNA4U73F

0.4 x 0.35 mm.

6.2.2 Tests on a single photodiode

A photodiode with integrated amplifier was placed on a breadboard and supplied with voltage $V_{cc} = 5V$, as indicated by the datasheet. It is written that the V_R resistance should be chosen between 0Ω and 800Ω. The tests were made with $V_R = 0\Omega, V_R = 220\Omega, V_R = 220\Omega{+}68\Omega$ in series and with $V_R = 470\Omega$. Empirically, we came to a conclusion that the larger values of V_R improve the sensitivity of the photodetector. This conclusion lead to the choice of $V_R = 470\Omega$ for the tests to follow.

As a next milestone, it was important to determine if it was possible to see the voltage changes with light intensity changes in the visible light wavelength region, before incorporating the diode in question into the final balanced detector design. Using the above mentioned setup, output voltage (V_{out}) was measured using an oscilloscope (Tektronix TDS 3014B) under different light conditions including only the ambient light, room with no natural or artificial light (apart from small sources such as a computer or the oscilloscope itself), and using a flashlight pointed directly onto the photodiode. The results of these measurements are shown in Table 6.2 :

Photodiode tests with $V_R = 470\Omega$	
Conditions	**Voltage (V)**
Dark room (lights out)	$1.40 - 1.48V$
Lights on	$1.40 - 1.48V$
Dark room + Flashlight	$1.56 - 1.74V$
Lights on + Flashlight	$1.56 - 1.68V$

Table 6.2: Photodetector tests

Surprisingly, there was no difference in voltage levels between photodiode in a room with ambient light and a photodiode in a dark room. As for the two cases with the flashlight, it can be seen that the voltage levels are pretty similar there as well, although the flashlight in a dark room resulted in a slightly higher maximum voltage. The voltage range is larger in cases where the flashlight was used, which together with the former statements, indicates that the light has to be pointed exactly onto the small photodetector area (0.4x0.35mm) for a relevant change in voltage to occur.

6.2.3 Testing the resulting signals of the optical setup using two photodiodes

Before continuing to the whole setup described in Chapter 4 (both optical setup and electronics), the concept had to be proven on the oscilloscope, in order to see whether the diodes were able to follow the high speed of the signal coming from the optical setup. Two optical fibers were placed on the photodiodes one and two respectively. Figure 6.7 shows the output of the first photodiode (in yellow), inverted output of the second photodiode (in blue). Sum of the two signals is shown (in red) using the "Math" function on an Agilent oscilloscope.

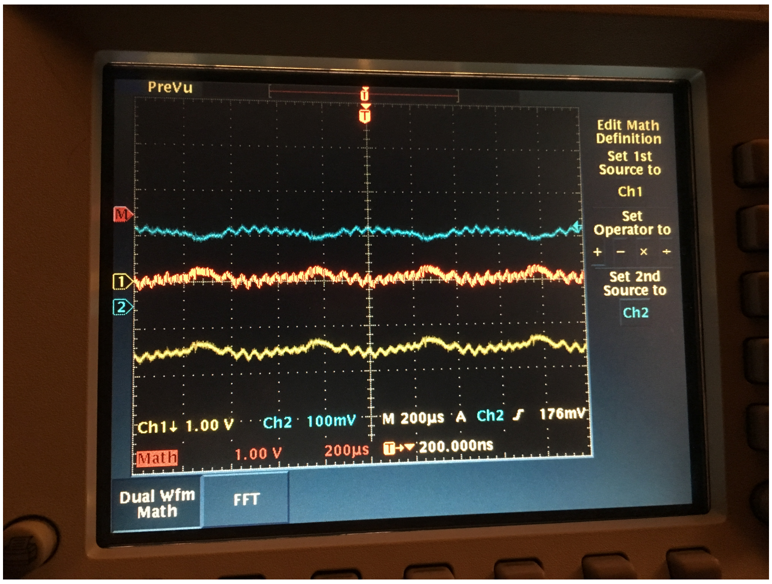

Figure 6.7: Balanced detection using two photodiodes: Results shown on an Oscilloscope

Ideally, the resulting sum should be close to zero, but in this case it looks extremely similar to signal from the first photodiode (in yellow). There are two most likely explanations for this phenomenon. Firstly, it could be a loose contact between the breadboard and wires of the second photodiode which should be controlling the output gain. Thus, even though the same resistors were placed to control the gain of both photodiodes, output signal of the first one would be stronger. Secondly, it could be that the signal coming out of the optical fiber was not aimed directly at the small light sensing area of the second photodiode.

6.2.4 Tests on Prototype 1

The setup that was described in chapter 4 was used for these tests. A mirror in the sample arm was chosen for the first tests as it should ideally reflect all the light back to the system, which facilitates the detection. In Figure 6.8 we can see the comparison between the Thorlabs balanced detector and our balanced detector prototype 1 with circuit built around instrumentation amplifier AD8221 used on the same sample. The upper graphs show the modulation, and the lower graphs show the position and amplitude of the signal sample signal.

It is noticeable that the signal intensity is significantly lower on both graphs when the custom photodetector is used. This can be explained by the extreme difficulty of manually aiming both optical fibers (reference and sample) to a really small detector area at the same time. However, the peak is exactly at the same position in both cases, meaning that the custom balanced detector measured the correct frequency form to the sample, which is essentially the most important information for ocular biometry. Also, note that even though the signal intensity is lower when using the custom balanced detector, the Signal-to-noise ratio stayed the same. This means that the noise level is also lower than the one provided by the commercial detector, which is very encouraging for further measurements.

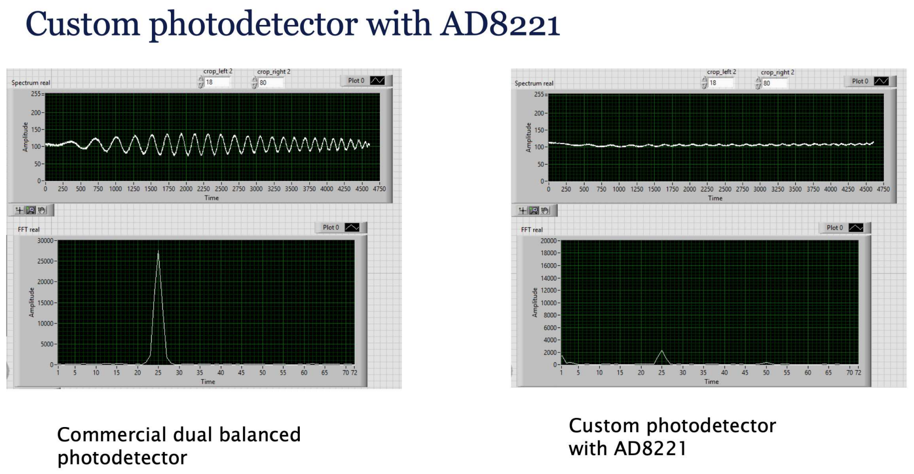

Custom photodetector with AD8221

Commercial dual balanced photodetector

Custom photodetector with AD8221

Figure 6.8: Sample:Mirror - Prototype 2 with AD8221

After the mentioned complications considering two fiber to photodiode connections, tests on the circuit built around the instrumentation amplifier AD8253 were made with single photodiode illumination, but dual balanced output, in order to remove the DC offset of the ambient light. Apart from the expected increase in noise, results shown in Figure 6.9 display promising results in terms of distance measurement, as was the case with the other circuit.

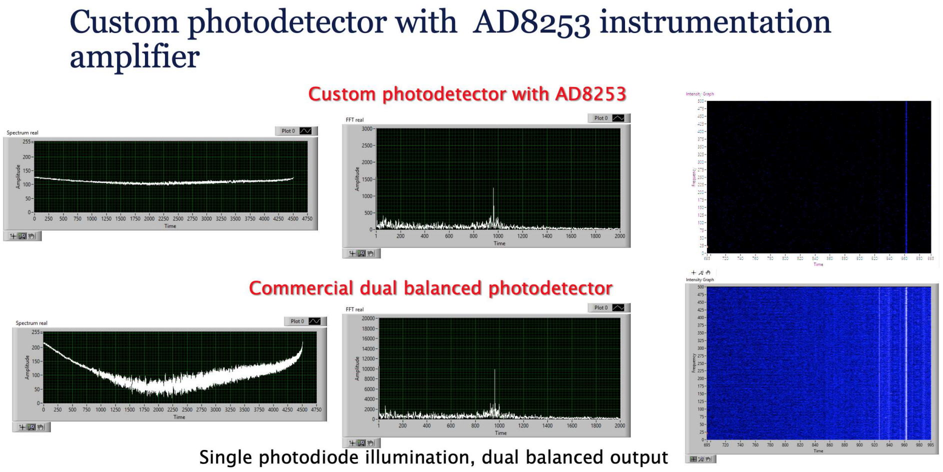

Custom photodetector with AD8253 instrumentation amplifier

Custom photodetector with AD8253

Commercial dual balanced photodetector

Single photodiode illumination, dual balanced output

Figure 6.9: Sample:Mirror - Prototype 1 with AD8253

6.2.5 Tests on Prototype 2

Encouraging results with prototype 1 lead to in-vivo measurements of the human eye with Prototype number 2 (with the circuit using instrumentation amplifier AD8221). This circuit was chosen because of the better control over the output gain (and larger variety of gain choices), since large scattering of the eye was to be expected. The result of these measurements is shown in Figure 6.10.

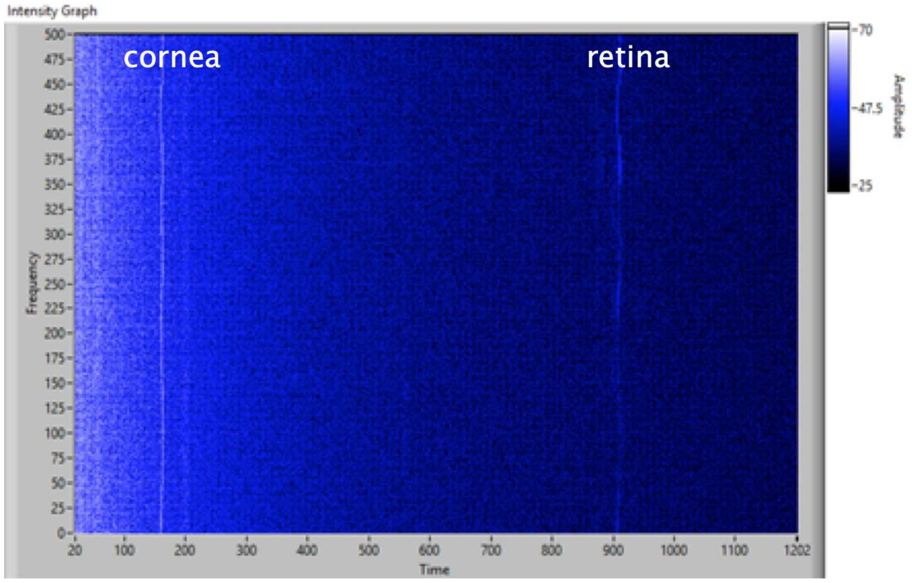

Figure 6.10: Sample:Human Eye - Prototype 2 with AD8221

The intensity graph undoubtedly shows concurrent peaks of both cornea and retina. The distance between the two interfaces is measured to be $d_{pixel} = 750 \pm 1$ pixel. In order of determining the geometrical distance between two peaks, it must be calculated from pixel values into SI-system units (m). This is done using the equation 6.2, with δz being a value in m corresponding to one pixel, λ_0 being the central wavelength of the VCSEL beam, and $\Delta\lambda$ being the tuning range of the VCSEL. Due to the noise in the beginning of the spectrum, part of the single sweep is cut off. As a result, the tuning range lowers from measured $\Delta\lambda = 8.5$ nm to $\Delta\lambda = 7.5$ nm for this measurement.

$$\delta z = \frac{2ln(2)}{\pi}\frac{\lambda_0^2}{\Delta\lambda} = \frac{2ln(2)}{\pi}\frac{850nm^2}{7.5nm} = 43\mu m \tag{6.2}$$

The obtained value δz (in m) corresponding to one pixel is then multiplied with the difference (measured in LabView) between the two interfaces to retrieve the optical distance (Equation 6.3):

$$d_{optical} = d_{pixel}\delta z = 32.25mm \pm 43\mu m \tag{6.3}$$

Finally, plugging $d_{optical}$ into equation 6.4 geometrical distance $d_{geometrical}$ is calculated.

$$d_{geometrical} = d_{optical}0.771 - 1.3617 = 23.50mm \pm 31\mu m \tag{6.4}$$

The value for $d_{geometrical} = 23.50$ mm ±31 μm is slightly lower than the value for the left eye of the same volunteer, determined using an IOL Master device, where $d_{geometrical}$ is measured to be 23.79 mm.

6.3 Compact System

6.3.1 Raspberry Pi speed tests

Output speed

The goal of the following test was to achieve the highest possible output speed of the Raspberry Pi 3B+ GPIO pins and measure it using an Agilent oscilloscope. Learning that interpreted languages like Python (which is one of the most popular programming languages in a raspberry Pi community) are slower than C, the idea of testing in python was abandoned at once. [1] Native C code with simply toggling an output pin of the GPIO was written with the goal of measuring the toggling speed. The result is shown in Figure 6.11. Note that the highest achieved frequency was measured to be 66.4 MHz. This number was by far larger than the frequency needed for current driving (which needs to be able to give out signals with 2 kHz).

---

[1] source: Huffpost.com

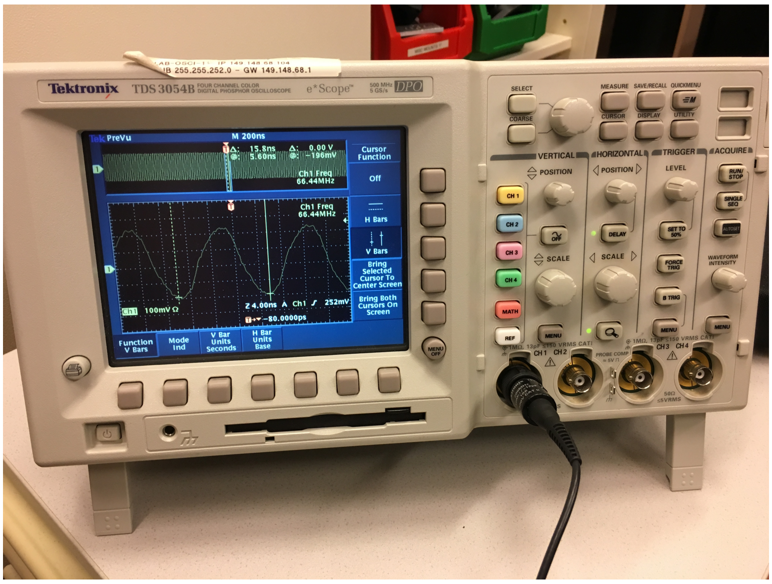

Figure 6.11: Raspberry Pi Output Speed Test

Input speed

To test the input speed of the Raspberry Pi 3B+ with GUI, different sinus signals were sent from a function generator, passing through an 8-bit A/D converter and coming onto the GPIO pins of the Raspberry Pi. Stamping the time on every voltage calculation, times 67-72 μs between two sampling values were obtained. This corresponds to frequencies of 13.89-14,71 kHz. The same test was then performed on a headless Raspberry Pi 3B+, this time with only zeros on the input GPIO pins. Only the time stamps were taken into account. This Raspberry Pi board was also equipped with an SD card with higher w/r rate (action camera SD card). The obtained values stayed at 68μs on the average, corresponding approx. 14 kHz.
With the goal of speeding up the input readings, changes in the program were made to optimize the calculation speed. For example, division takes more time than multiplication. Hence, division by 255 was substituted with multiplication by 0.003921568627, even though this will worsen the precision of the calculated voltage levels. Regardless of the optimizations, the results stayed the same with 68 μs on the average.
Using the C code mentioned above, sinus signals of different frequencies (10 kHz, 100 kHz, 500 kHz, 1 MHz and 5 MHz) were generated using a functions generator and sent through the A/D converter (Texas Instruments ADC1173) to the input pins on the GPIO of the Raspberry Pi 3B+. The obtained data is represented graphically in figure 6.12.
Since we learned that the acquisition frequency of the input signals on the raspberry pi with the program we used was approximately 14 kHz, the obtained

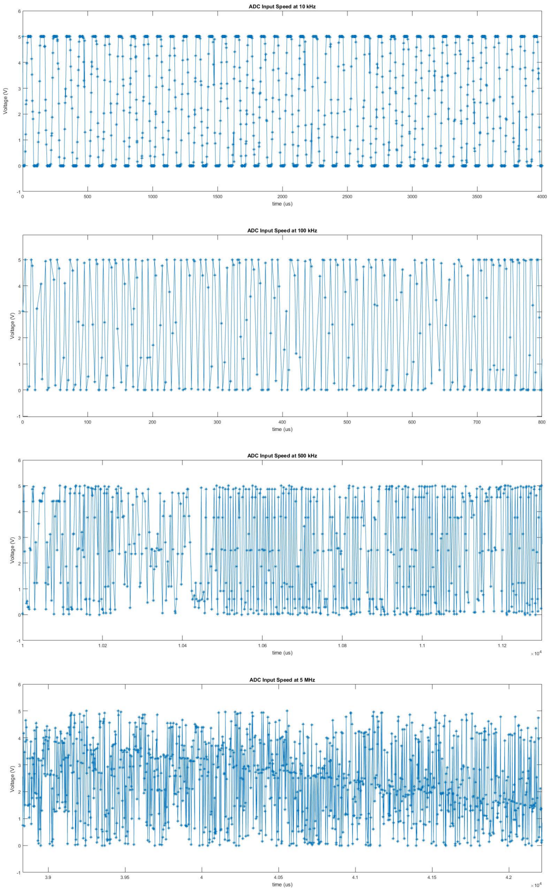

Figure 6.12: ADC speed tests with sinus signals of $10kHz$, $100kHz$, $500kHz$ and $5MHz$ on GPIO input

results were expected, especially since the Nyquist–Shannon sampling theorem states that this frequency should be at least double the frequency of the signal. Note how the graph with the sinus signal of 5 MHz shows a nice example of aliasing effects (Figure 6.13).

Stability

Another important point in a choice of the controller device was the stability in signal acquisition. We had to be certain that the device (in this case a raspberry microcomputer) will not prioritise other background processes over signal acquisition on the GPIO input pins, which could lead to losses of parts of the signal we wish to obtain.
Figure 6.13 shows some concerning results regarding the acquisition stability. As we can see the data for some time stamps is simply not present, regardless of the fact that the program was running without break for a short period of

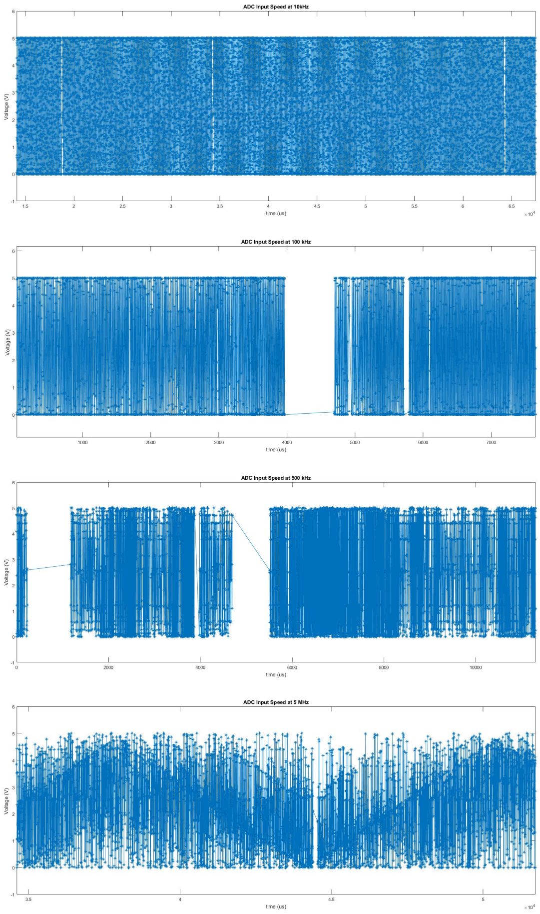

Figure 6.13: Stability test overviews with sinus signals of $10kHz$, $100kHz$, $500kHz$ and $5MHz$ on GPIO input

time. This was the main reason it was decided to abandon Raspberry Pi as a solution for the ADC control and input data acquisition device.

6.3.2 Testing the ADC with Texas Instruments board

The chosen ADC was Texas Instruments ADC1173. It is an 8-bit parallel ADC with the highest conversion speed of 15Msps. The cost of the ADC is approx. 3.5 € (according to digikey.de). It can be run by an external clock, which would theoretically provide a chance for synchronization with other electronic devices in a compact system run by a single microcomputer.

With the aim of simplifying the testing a corresponding evaluation board was used (cost approx. 140 € according to digikey.de). The board in question is shown in Figure 6.14[2]. Output voltage of its bits is at a high level is 5V, meaning the signals would have to be lowered using a voltage divider circuit before entering the input pins of the Raspberry Pi GPIO.

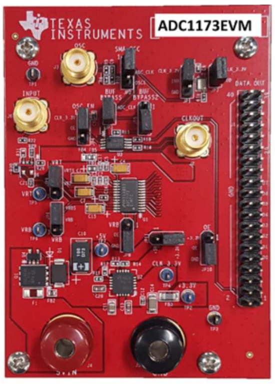

Figure 6.14: ADC1173 Evaluation Board

Testing the ADC with Texas Instruments board

Because of the results concerning the acquisition instability of the Raspberry Pi microcomputer, already available Texas Instruments TSW1400 Data converter evaluation module was used from this moment on to provide a connection between the ADC and a PC. The corresponding software called "High Speed Data Converter Pro" was used for visualizing the acquisition results.

To test the functionality of the adc-tsw1400 board-pc connection, a 5MHz sinusoidal signal was sent using a waveform generator. The results are shown in Figure 6.15 in frequency domain. The software can visualise the results in time or frequency domain.
The next tests were made on the optical setup, using the Thorlabs balanced detector and a test eye (with 85dB signal loss) as a sample. Figure 6.16 shows a single sweep first in LabView environment using the original setup, and the same sweep in time domain of the High speed data conversion software.
The results were unclear from the previous figures, which is why it had to be tested whether the biometric data can be obtained using this ADC. The binary data was extracted from the high speed data acquisition software and was processed in Matlab. A Matlab script[3] was used to try and reconstruct the signals of the two interfaces of the test eye (cornea and retina).
The extracted signals have to be relinearized using the phase relinearization algorithm for multiple reflections. This method works only if the relection peaks are clearly separated.

---

[2] source: www.ti.com

[3] The existing script in use is a courtesy of Dr Ferrara and DI Niederleithner

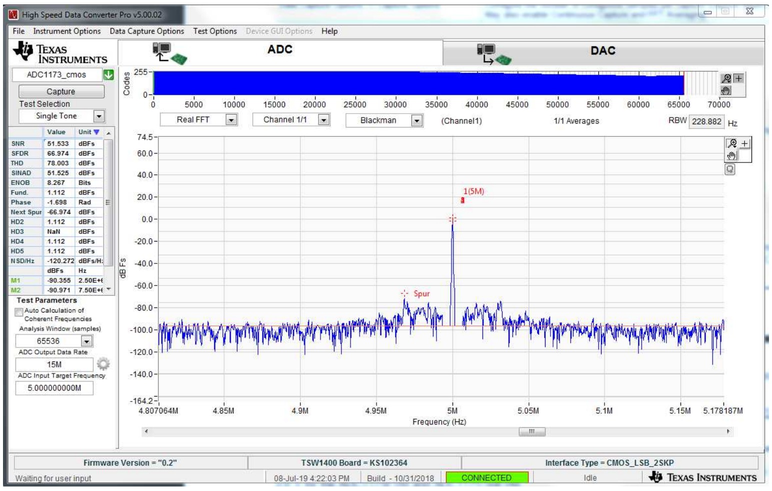

ADC1173_cmos

Test Selection: Single Tone

	Value	Unit
SNR	51.533	dBFs
SFDR	66.974	dBFs
THD	78.003	dBFs
SINAD	51.525	dBFs
ENOB	8.267	Bits
Fund.	1.112	dBFs
Phase	-1.698	Rad
Next Spur	-66.974	dBFs
HD2	1.112	dBFs
HD3	NaN	dBFs
HD4	1.112	dBFs
HD5	1.112	dBFs
NSD/Hz	-120.272	dBFs/H:
	dBFs	Hz
M1	-90.355	2.50E+(
M2	-90.971	7.50E+(

Test Parameters

☐ Auto Calculation of Coherent Frequencies

Analysis Window (samples): 65536

ADC Output Data Rate: 15M

ADC Input Target Frequency: 5.000000000M

Real FFT

Channel 1/1

Blackman

(Channel1)

1/1 Averages

RBW 228.882 Hz

Firmware Version = "0.2"

TSW1400 Board = KS102364

Interface Type = CMOS_LSB_2SKP

Waiting for user input

08-Jul-19 4:22:03 PM

Build - 10/31/2018

CONNECTED

Idle

Figure 6.15: ADC functionality test

1. Isolate a single sweep from the acquired signal
2. Obtain a spectrum of the chirped signal. Rather than seeing peaks of the eye interfaces, the Fourier signal is a broadened contribution
3. Cut the first peak out

   One peak is cut out under the assumption that the non-linearities will be the same for all other peaks, since the light source is the same. It is speculated that if one peak is remapped correctly, other peaks will appear/improve as well.

4. Extract the phase
5. Remap the signal with phase information using interpolation.
6. Relinearize the signal.

The intermediate steps are visualized in Figure 6.17. It can be concluded that both cornea and retina peeks were successfully reconstructed.

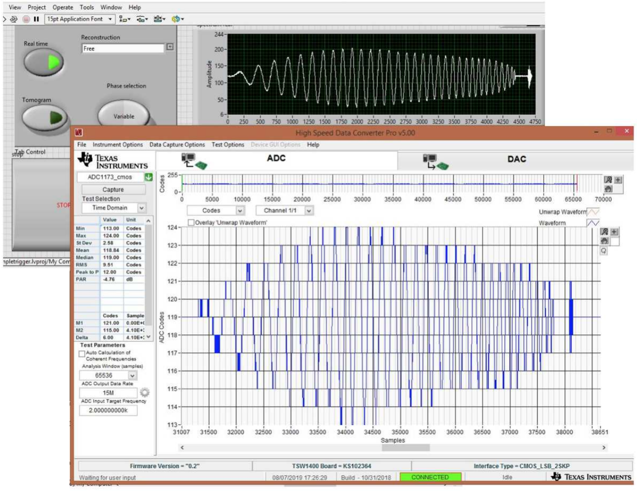

ADC1173_cmos

Test Selection: Time Domain

	Value	Unit
Min	113.00	Codes
Max	124.00	Codes
St Dev	2.58	Codes
Mean	118.84	Codes
Median	119.00	Codes
RMS	9.51	Codes
Peak to P	12.00	Codes
PAR	-4.76	dB

	Codes	Sample
M1	121.00	0.00E+
M2	115.00	4.10E+
Delta	6.00	4.10E+

Test Parameters

☐ Auto Calculation of Coherent Frequencies

Analysis Window (samples): 65536

ADC Output Data Rate: 15M

ADC Input Target Frequency: 2.000000000k

Reconstruction: Free

Firmware Version = "0.2"
TSW1400 Board = KS102364
Interface Type = CMOS_LSB_2SKP
Waiting for user input
08/07/2019 17:26:29
Build - 10/31/2018
CONNECTED
Idle

Figure 6.16: LabView vs. High Speed Data Conversion Software: Single sweep in Time domain

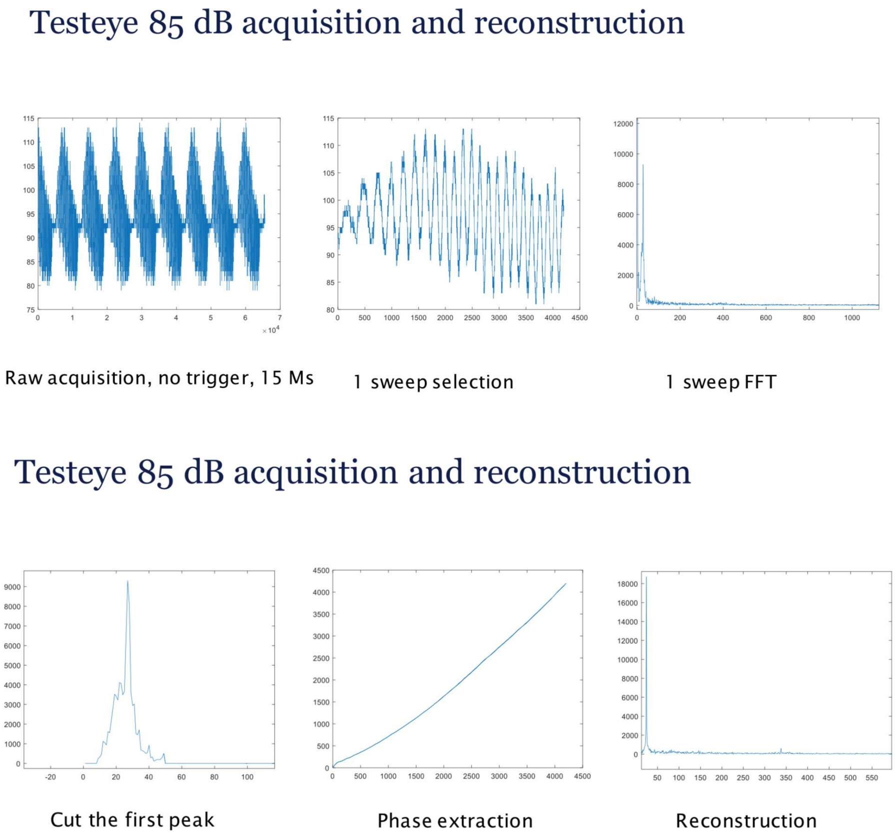

Testeye 85 dB acquisition and reconstruction

Raw acquisition, no trigger, 15 Ms

1 sweep selection

1 sweep FFT

Testeye 85 dB acquisition and reconstruction

Cut the first peak

Phase extraction

Reconstruction

Figure 6.17: Matlab: Intermediate steps in signal reconstruction

Chapter 7

Discussion

This thesis had three main goals: providing an economic solution for the driver of the electronically-tuned VCSEL source, designing a custom-made balanced detector and developing a compact system, that would control the performance of both source and detector electronics.

The first goal was selecting an economic solution for the driver of the electronically-tuned VCSEL source, and testing its performance in comparison to the Newport current driver currently in use. Results have shown that the Analog Technologies electronic module that was chosen as a laser diode driver was able to achieve exactly the same tuning range as the commercial Newport driver, for only a portion of the consumed power.

Grulkowski et al.[29] demonstrated that the swept-source OCT in combination with VCSEL technology can be used to perform high-precision non-contact ocular biometry. Similarly to Grulkowski et al., we have concluded that a swept-source VCSEL provides sufficient precision for ocular biometry. However, contrary to their conclusion, we believe that SS-VCSELs have a potential for performing OCT scanning to some extent, given that a satisfactory tuning range is achieved. Another solution for improving the low-bandwidth scanning results would be further research into state of the art post-processing techniques.

The second goal was designing a custom-made balanced detector that can provide reasonably good results for high-speed signals in ophthalmic biometry. The created detector was then compared with a commercial Thorlabs balanced detector currently in use. Our results have shown that a custom-made board has the potential to be used as a balanced detector and perform with sufficient efficiency by capturing both signals of cornea and retina in-vivo.

The in-vivo measurement of axial length of a healthy volunteer has resulted in a discrepancy of approximately 300 μm between a low cost biometry setup with a custom balanced detector and IOL Master 500 device, which is considered to be a gold standard in optical biometry. This difference may be a consequence of a inaccurate estimation of the VCSEL tuning range, since a single sweep interval is elected manually, and may therefore not be determined with precision. Further studies have to be conducted on a larger number of subjects, to obtain more information about the precision of the measurements with a custom balanced detector.

The third goal was designing a compact system, controlled by a single board, that would manage the performance of both source and detector electronics, thus making the use of the desktop computer obsolete in these measurements. This would have conceivably ensured the possibility of creating a portable economic device for eye-length measurements available to anyone. Results have shown that a Raspberry Pi 3B+ microcomputer alone is not well-suited to perform these tasks, due to instability in signal acquisition and an insufficient GPIO input speed. However, it remains to be determined whether a microcomputer in combination with one or two high speed microcontrollers would be better suited to perform this tasks and ensure the portability of the system.

Tivnan at al.[30] encountered a similar problem when trying to acquire a digital input signal of 5-20 MHz using the Raspberry Pi GPIO. An uninterrupted acquisition of the signal at the GPIO input pins could not be achieved using the default Linux operating system provided by the Raspberry Pi. They concluded that this was most likely due to the multi-tasking nature of the operating system in question.

All in all, regarding the cost-cutting strategy in electronics, as we can see in Figure 7.1, total costs of electronic devices used in this system have lowered from 4700 € to 2400 € for system electronics. This is a promising development that gives hope that this system can become economically accessible to developing countries as well.

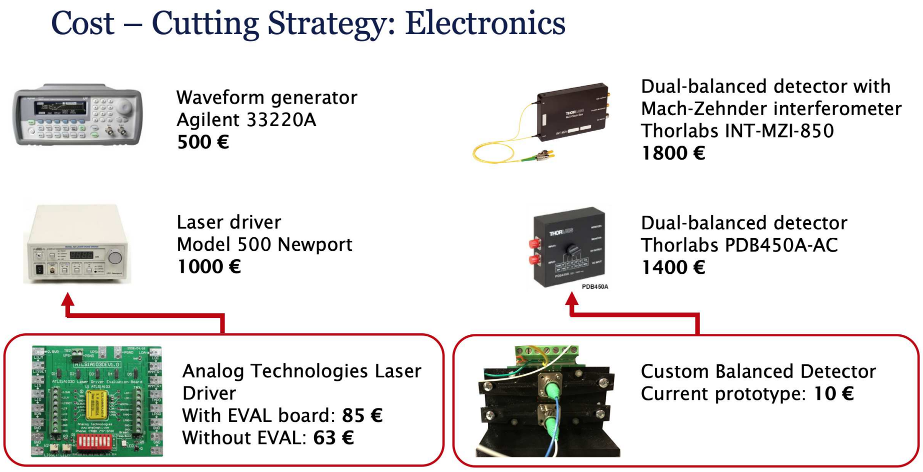

Cost – Cutting Strategy: Electronics

Waveform generator
Agilent 33220A
500 €

Dual-balanced detector with
Mach-Zehnder interferometer
Thorlabs INT-MZI-850
1800 €

Laser driver
Model 500 Newport
1000 €

Dual-balanced detector
Thorlabs PDB450A-AC
1400 €

Analog Technologies Laser Driver
With EVAL board: **85 €**
Without EVAL: **63 €**

Custom Balanced Detector
Current prototype: **10 €**

Figure 7.1: Cost-cutting strategy: summary

Chapter 8

Conclusions

1. Electrically pumped swept-source VCSEL provides a satisfactory tuning range for performing ocular biometry.
2. Analog Technologies low-cost laser driver electronic module and commercial laser drivers perform electrical tuning of a VCSEL equally well. In addition, low-cost laser driver operates with a smaller power consumption.
3. Custom balanced detector circuit is fit for carrying out axial-length measurements in optical biometry.
4. When creating a system run by a microcomputer, Raspberry Pi 3B+ board has proven to be an inadequate choice, due to the instability in data acquisition.

Chapter 9

Outlook

Future work will concentrate on performing the mentioned tests with the balanced detector on a printed circuit board. The research should show whether the noise reduction, that it would theoretically provide, suffices for seeing the eye lens signals as well as the the cornea and retina signals.

Furthermore, it should be considered whether the two hardware devices presently used in the system could be replaced by more compact and inexpensive alternatives. For example our custom balanced detector circuit could potentially be expanded to include a part of the circuit that would replace the Thorlabs balanced detector that uses the Mach-Zehnder interferometer (used in fiber setup). Another idea would be to substitute the waveform generator with a microcontroller for instance.

In addition, it remains to be explored whether a better choice of a microcomputer/microcontroller system can be used to create a system not dependant on a personal computer, that would result in portability and further economical accessibility of this biometric system.

List of Figures

List of Tables

Bibliography

[1] Efraim Jaul and Jeremy Barron. Age-related diseases and clinical and public health implications for the 85 years old and over population. *Frontiers in Public Health*, 5, December 2017.

[2] Cameron M. Lee and Natalie A. Afshari. The global state of cataract blindness. *Current Opinion in Ophthalmology*, 28(1):98–103, January 2017.

[3] Tiago B. Ferreira, Kenneth J. Hoffer, Filomena Ribeiro, Paulo Ribeiro, and João G. O'Neill. Ocular biometric measurements in cataract surgery candidates in portugal. *PLOS ONE*, 12(10):e0184837, October 2017.

[4] Manuel Garza-Leon, Hugo A. Fuentes de la Fuente, and Ana V. Garcia-Trevino. Repeatability of ocular biometry with iolmaster 700 in subjects with clear lens. *International Ophthalmology*, 37(5):1133–1138, October 2016.

[5] Galia Adler, Jonathan Shahar, Rivka Kesner, Eldar Rosenfeld, Naomi Fischer, Anat Loewenstein, and Shimon Kurtz. Effect of pupil size on biometry measurements using the iolmaster. *American Journal of Ophthalmology*, 159(5):940–944, May 2015.

[6] Ahmet Akman, Leyla Asena, and Sirel Güngör. Evaluation and comparison of the new swept source oct-based iolmaster 700 with the iolmaster 500. *British Journal of Ophthalmology*, 100(9):1201–1205, December 2015.

[7] Nino Hirnschall, Ralph Varsits, Birgit Doeller, and Oliver Findl. Enhanced penetration for axial length measurement of eyes with dense cataracts using swept source optical coherence tomography: A consecutive observational study. *Ophthalmology and Therapy*, 7(1):119–124, March 2018.

[8] Sucbei Moon and Eun Seo Choi. VCSEL-based swept source for low-cost optical coherence tomography. *Biomedical Optics Express*, 8(2):1110, January 2017.

[9] Ming-Zher Poh, Daniel McDuff, and Rosalind Picard. A medical mirror for non-contact health monitoring. In *ACM SIGGRAPH 2011 Emerging Technologies on - SIGGRAPH '11*. ACM Press, 2011.

[10] K. P. Mashige. A review of corneal diameter, curvature and thickness values and influencing factors. *African Vision and Eye Health*, 72(4), December 2013.

[11] Allen O. Eghrari, S. Amer Riazuddin, and John D. Gottsch. Overview of the cornea. In *Progress in Molecular Biology and Translational Science*, pages 7–23. Elsevier, 2015.

[12] Lee Ann Remington. *Clinical Anatomy of the Visual System*. Elsevier, 2005.

[13] P J Foster. Risk factors for nuclear, cortical and posterior subcapsular cataracts in the chinese population of singapore: the tanjong pagar survey. *British Journal of Ophthalmology*, 87(9):1112–1120, September 2003.

[14] Elena Prokofyeva, Alfred Wegener, and Eberhart Zrenner. Cataract prevalence and prevention in europe: a literature review. *Acta Ophthalmologica*, 91(5):395–405, June 2012.

[15] A. Haripriya, H. Sonawane, and R. D. Thulasiraj. Changing techniques in cataract surgery: how have patients benefited? *Community Eye Health*, 30(100):80–81, 2017.

[16] Fouad R. Nakhli. Comparison of optical biometry and applanation ultrasound measurements of the axial length of the eye. *Saudi Journal of Ophthalmology*, 28(4):287–291, October 2014.

[17] Veena Bhardwaj. Axial length, anterior chamber depth-a study in different age groups and refractive errors. *Journal of Clinical and Diagnostic Research*, 7(10):2211–2212, 2013.

[18] Matthew T. Feng, Michael W. Belin, Renato Ambrósio, Satinder P.S. Grewal, Wang Yan, Mohamed S. Shaheen, Charles McGhee, Naoyuki Maeda, Tobias H. Neuhann, H. Burkhard Dick, Saleh A. Alageel, and Andreas Steinmueller. Anterior chamber depth in normal subjects by rotating scheimpflug imaging. *Saudi Journal of Ophthalmology*, 25(3):255–259, July 2011.

[19] Jim Schwiegerling. *Field Guide to Visual and Ophthalmic Optics (SPIE Vol. FG04)*. SPIE Publications, November 2004.

[20] Fujimoto J. Drexler W. *Optical Coherence Tomography: Technology and Applications*. Springer, 2015.

[21] J. A. Izatt and M. A. Choma. *Theory of Optical Coherence Tomography*, pages 47–72. Springer Berlin Heidelberg, Berlin, Heidelberg, 2008.

[22] S. H. Yun and B. E. Bouma. *Wavelength Swept Lasers*, pages 359–377. Springer Berlin Heidelberg, Berlin, Heidelberg, 2008.

[23] J.L. Jewell, J.P. Harbison, A. Scherer, Y.H. Lee, and L.T. Florez. Vertical-cavity surface-emitting lasers: Design, growth, fabrication, characterization. *IEEE Journal of Quantum Electronics*, 27(6):1332–1346, June 1991.

[24] Harry Dutton. *Understanding Optical Communications*. Prentice Hall, 1998.

[25] Samiha Ishrat Islam, Arnob Islam, and Saiful Islam. Integrated duo wavelength VCSEL using an electrically pumped GaInAs/AlGaAs 980 nm cavity at the bottom and an optically pumped GaInAs/AlGaInAs 1550 nm cavity on the top. *International Scholarly Research Notices*, 2014:1–10, 2014.

[26] K.D. Choquette. Vertical cavity surface emitting lasers (VCSELs). In *Semiconductor Lasers*, pages 316–340. Elsevier, 2013.

[27] C. Hagart-Alexander. Temperature measurement. In *Instrumentation Reference Book*, pages 269–326. Elsevier, 2010.

[28] Reinhard Lerch. *Elektrische Messtechnik*. Springer Berlin Heidelberg, 2016.

[29] Ireneusz Grulkowski, Jonathan J. Liu, Jason Y. Zhang, Benjamin Potsaid, Vijaysekhar Jayaraman, Alex E. Cable, Jay S. Duker, and James G. Fujimoto. Reproducibility of a long-range swept-source optical coherence tomography ocular biometry system and comparison with clinical biometers. *Ophthalmology*, 120(11):2184–2190, November 2013.

[30] Matthew Tivnan, Rajan Gurjar, David Wolf, and Karthik Vishwanath. High frequency sampling of ttl pulses on a raspberry pi for diffuse correlation spectroscopy applications. *Sensors*, 15(8):19709–19722, August 2015.